*aerospace*

MDPI

*Article*

# Dynamic Modeling and Vibration Suppression of a Rotating Flexible Beam with Segmented Active Constrained Layer Damping Treatment

**Yue Wang [1,†], Yiming Fang [1,†], Liang Li [1,*], Dingguo Zhang [1], Wei-Hsin Liao [2] and Jianshi Fang [3]**

[1] School of Physics, Nanjing University of Science and Technology, Nanjing 210094, China; yuewang@njust.edu.cn (Y.W.); fangyiming99@njust.edu.cn (Y.F.); zhangdg419@mail.njust.edu.cn (D.Z.)
[2] Department of Mechanical and Automation Engineering, The Chinese University of Hong Kong, Shatin, NT, Hong Kong, China; whliao@cuhk.edu.hk
[3] School of Materials Science and Engineering, Nanjing Institute of Technology, Nanjing 211167, China; fangjsh@njit.edu.cn
* Correspondence: liangli@njust.edu.cn
† These authors contributed equally to this work.

**Abstract:** This paper uses high-order approximate coupling (HOAC) dynamics equations for the hub–beam system with segmented active constrained layer damping treatment (SACLD). To improve the damping characteristics of traditional active constrained layer damping (ACLD), the viscoelastic damping layer, and the piezoelectric constraining layer are cut at the same position. The damping characteristics of the structure are enhanced by increasing the shear strain of the viscoelastic damping layer. The finite element method is used to discretize the SACLD beam. The discontinuity of the SACLD beam element-to-element displacement achieves the notch. Based on the theory of rigid–flexible coupling dynamics, the dynamic responses of the SACLD rotating beam under different cases are studied. The results show that the segmentation method is not always effective. A SACLD beam provides better vibration suppression than an ACLD beam only when appropriate material and dimensional parameters are used. The influences of base-layer thickness, piezoelectric constraining layer thickness, viscoelastic damping-layer thickness, angular velocity, the viscoelastic damping-layer loss factor, and control gains on the vibration of the rotating flexible beam with SACLD treatment are also discussed.

**Keywords:** segmented active constrained layer damping; rigid-flexible coupling; dynamic modeling; finite element method; vibration control



**Citation:** Wang, Y.; Fang, Y.; Li, L.; Zhang, D.; Liao, W.-H.; Fang, J. Dynamic Modeling and Vibration Suppression of a Rotating Flexible Beam with Segmented Active Constrained Layer Damping Treatment. *Aerospace* **2023**, *10*, 1010. https://doi.org/10.3390/aerospace10121010

Academic Editor: Rosario Pecora

Received: 31 October 2023
Revised: 20 November 2023
Accepted: 25 November 2023
Published: 30 November 2023



## 1. Introduction

With the rapid development in the field of manned space, the issue of the space robotic arm has received considerable critical attention. The space flexible robotic arm can solve the problem of out-of-bay operation to a certain extent; it can perform space-operation tasks through in-orbit manipulation, ground teleoperation, or autonomous operation. After unfolding in space, the robotic arm has the characteristics of small structural damping and low and concentrated modal frequencies. The long-time vibration of the robotic arm increased the cost of spaceflight work. At the same time, the coupling of the motion attitude variation of a spacecraft's rigid main structure and the flexible structure's own motion would produce unfavorable nonlinear vibration. So, it is of great importance to study the vibration suppression of the robotic arm. Segmented active constrained-layer damping (SACLD) beams are not only beneficial for research on space robotic arms but also have applications in aviation, specifically for rotating blades and turbofans. Vibrations in these components can lead to damage and decreased performance. SACLD has the potential to mitigate these vibrations, thereby extending component lifespan and reducing maintenance needs. Furthermore, by minimizing vibration in turbofan engines, SACLD

can enhance their efficiency and lessen noise, which are critical factors in the development of environmentally friendly aircraft.

There are passive control methods for the vibration control of spatially flexible structures. Common passive control methods include passive constrained layer damping (PCLD), which attaches a viscoelastic material (VEM) to the surface of the structure and covers the VEM with a further elastic constrained layer (CL). Ma et al. [1] introduced the effect of constrained-layer damping (CLD) on structural vibration into the nonlinear model of the bolt. The nonlinear vibration characteristics of a double cylindrical shell with partially attached CLD bolts under substrate excitation were investigated using a semianalytical method. And the experiments are designed to verify the reasonableness of the model. Li et al. [2] proposed a new analytical model to accurately predict the strain-dependent properties of partially constrained layer damping (CLD) treatments of fiber-reinforced composite shells. The effect of the material properties on the nonlinear vibration behavior of the partially CLD patch cover was also studied. Cai et al. [3] proposed a vibration-response analysis method for a beam partially covered with PCLD treatment. This method can describe the vibration response of the VEM layer more accurately. Zheng et al. [4] investigated the effect of covering multiple PCLD patches on beams and the distance between the patches on the structure's damping characteristics. They also studied cylindrical shells with PCLD treatment and proposed an optimization method to lay out PCLD patches [5]. Zheng et al. [6] investigated the vibration-damping characteristics of multilayer PCLD-treated cylindrical shells using the semianalytic transfer matrix method. Zhang and Sainsbury [7] applied the Galerkin element method (GEM) to the vibration problem of plates with PCLD treatment, and the results showed that GEM has high computational efficiency for plates with PCLD treatment. Gröhlich et al. [8] proposed a new optimization approach of treating the layer widths of the CLD structure as design parameters, demonstrating a significant increase in damping.

Due to the lack of control flexibility and the limited damping capacity of the passive control method, it is more effective for high-frequency vibration suppression but not for low-frequency vibration control. Baz and Ro [9] replaced the elastic constraining layer in the conventional PCLD system with a piezoelectric constraining layer and an active constrained damping layer (ACLD); an integrated active–passive vibration-control method can be obtained. Baz also detailed the basic principles of passive and active damping techniques and used smart materials to enhance the vibration damping for passive treatment [10]. Varadan et al. [11] developed a three-dimensional finite element closed-loop model to predict the effects of rotating structures with ACLD treatment. The results showed that ACLD provides better vibration suppression than the PCLD structures. Fung and Yau [12] studied the vibration characteristics of a clamping-free rotating flexible robotic arm with fully covered ACLD treatment using the finite element method discretization. They analyzed the effects of different rotational speeds, thickness ratios, loss factors, and controller gains on the structural frequencies and damping ratios. Lee [13] explored the use of ACLD to control the vibration and acoustics of the beam by maximizing the loss factor, significantly reducing the resonant response. Sharnappa et al. [14] researched the active vibration control of composite beams in thermal environments, revealing the influences of thermal dependence and fiber orientation on system dynamics. Vasques and Rodrigues [15] covered both sides of the beam with multilayer elastic, piezoelectric, and viscoelastic layers. They performed numerical simulations of structures with feedback, adaptive feedback, and hybrid control systems. Boudaoud et al. [16] proposed an analytical method for the damping analysis of sandwich beams with piezoelectric and viscoelastic layers, providing an analytical expression for damping analysis. Kumar and Singh [17] made different samples of beams with ACLD and PCLD treatments to investigate the ACLD and PCLD patch positions and coverage by experiment. Kumar and Kumar [18] performed theoretical and experimental vibration analyses of rotating beams with added ACLD and stress-layer damping treatment. Panda et al. [19] investigated using active fiber-composite (AFC) materials for ACLD treatment to control vibrations of functionally graded (FG) beams.

Li et al. [20] derived higher-order approximate coupled dynamics equations for a rotating beam with ACLD treatment, which could be used to study an extensive range of rotation of the system considering dynamic stiffening effects. Guo et al. [21] evaluated the vibration characteristics of the beam with ACLD treatment in the temperature field. They analyzed the thermal vibration characteristics of the system in both closed-loop and open-loop cases. Mishra and Sarangi [22] researched the use of viscoelastic composite material (VECM) for ACLD treatment to enhance the damping characteristics. Li et al. [23] applied proportional feedback control to achieve vibration-reduction control of an ACLD cantilever beam. They studied the effect of the control-signal phase on the vibration-suppression effect of ACLD cantilever beams and determined the impact of the control-signal phase on the vibration reduction effect by establishing an experimental platform and a dynamic model. Based on investigations of flexible beams with ACLD treatment, Park and Baz [24] conducted vibration-control studies on plates covered with ACLD. Li et al. [25] performed a free vibration analysis for the significant rotation of plates with fully covered ACLD treatment. The results showed that dynamic stiffening and dynamic softening effects occurred when the flexible plate underwent rigid body motions. In addition, researchers covered ACLD on composite plates, such as multi-iron fiber-composite plates [26], graphene-reinforced material composite plates [27], plates with carbon-nanotube-reinforced composite cores [28], etc. Zhao et al. [29] proposed an equivalent single-layer simplification method to simulate plates covered with a constrained damping layer, which can reduce computational costs and maintain accuracy. Zhai et al. [30] investigated the vibration-control problem of an aviation piping system using ACLD treatment. A three-dimensional finite element model of the pipeline with ACLD patches is developed. Zhang et al. [31] studied the vibration and damping effect of an ACLD pipe with fixed support. The equations of motion of the ACLD pipe were established using the finite element method. Vinyas [32] investigated the effect of ACLD on the linear frequency response characteristics of tilted magnetoelectric elastic plates. Vinyas et al. also used a finite element method to evaluate the effect of ACLD treatment on the accurate control of the frequency response of functional gradient oblique functionally graded skew-magneto-electro-elastic plates [33].

For traditional ACLD structures, a viscoelastic damping layer would lead to poor active control transfer from the piezoelectric constraining layer to the primary controlled system, resulting in more controlled energy consumption. To improve the active control energy efficiency of the ACLD, Liao and Wang [34–36] invented a new enhanced active constrained layer damping (EACLD) structure by attaching edge elements to each end of the PZT layer and established the equivalent rigid spring mechanical model. The superiority of EACLD over conventional ACLD was verified experimentally. Gao and Liao [37] developed an energy-based approach to investigate the damping characteristics of beams treated with enhanced self-sensing active constrained layer (ESACL) damping. They found that edge elements in ESACL significantly improve the system-damping performance, with boundary conditions playing a crucial role. Jin et al. [38] applied EACLD to a hub-flexible rotating beam considering the stiffness of the edge element and the point mass. Li et al. [39] studied a flexible rotating beam with partially covered EACLD treatment in both open-loop and closed-loop cases. Fang et al. [40] considered the temperature field based on the EACLD beam model and replaced the material of the base beam with functionally graded materials for the study. Gupta et al. [41] used an in-house finite element model to study a carbon nanotube-based hybrid carbon fiber-reinforced smart beam. They found that the integration of carbon nanotubes into the epoxy matrix significantly enhances the damping performance, indicating the potential for efficient, high-performance, and lightweight micro-electromechanical systems. Jiang et al. [42] investigated the rotating-plate model with the EACLD treatment and a performed vibration analysis on the coverage area and coverage location of the EACLD patch. They also designed a combinatorial neural network to investigate the vibration estimation of rotating flexible plates treated with EACLD treatment and the vibration-suppression capability of composite structures under different operating conditions [43].

In addition to the EACLD structure, an improvement to the traditional constrained layer damping structure is segmented active constrained layer damping (SACLD). SACLD cuts off both the constrained and viscoelastic damping layers to improve the damping characteristics of the system by creating a region of concentrated shear displacement at the segment location. Plunkett and Lee [44] were the first to investigate segmented constrained layer damping. They were based on PCLD and only cut the constrained layer to increase the damping characteristics. Kress [45] found that the shear displacement concentration effect in the constrained damping layer is concentrated at the end of the beam, which is called the "edge effect". So, he proposed to cut off the constrained layer and the constraining layer at the same time. The constrained layer will produce a high-shear region at the cut-off location, called the "notch effect". This method can improve the damping characteristics of the constrained damping-layer structure. Studies by Lesieutre and Lee [46] demonstrated that segmented active constrained layer damping treatment is more robust than continuous processing. Kapadia and Kawiecki [47] experimentally investigated the effect of segmented active constrained layer damping treatment on the damping of flexible beams. It was found that damping improvement at lower natural frequencies was substantially more significant than at high natural frequencies. Trompette and Fatemi [48] conducted a study based on PCLD by cutting off both the constrained layer and the constraining layer and applying only one cut to the beam, analyzed the effect of the cut location on the structural vibration, and optimized the cut location using a simple genetic algorithm. Liu et al. [49] applied segmented constrained layer damping to a box beam of a helicopter to improve the helicopter's aerodynamic stability. Chattopadhyay et al. [50] used a mixed displacement field to model segmented constrained layer damping treatment. Cento and Kawiecki [51] have introduced a new finite element tool for analyzing segmented active constrained layer damping treatments applied in bending. They validated the significant impact of constraining layer strains on the damping ratios at basic modal frequencies and experimentally verified the model's effectiveness. Al-Ajmi and Bourisli [52] used a genetic algorithm to optimize the geometric parameters of the structure as well as the number and location of the cuts. Grégoire and Gerald [53] developed an optimization algorithm using mathematical programming to determine a segment arrangement that would yield an optimal loss factor. Avinash and Pravin [54] reviewed the literature on the optimal design of SACLD, guiding the optimization of the segmentation of viscoelastic materials in composite structures. Tian et al. [55] analyzed the effectiveness of the segmentation method. They showed that the segmentation method only applies to low shear-strain levels within the viscoelastic layer. Chinonso [56] applied SACLD to beams and sinusoidal structures and modeled them with 3D printing to investigate the characteristics of SACLD.

To the best of the authors' knowledge, no one has applied SACLD processing to rotating flexible beam structures in the existing literature. Therefore, this paper uses a floating frame-of-reference method to analyze the vibration control of a flexible rotating beam with fully covered SACLD treatment in both open-loop and closed-loop cases. Section 2 uses the finite element method to discretize the SACLD beam. The dynamics of the hub beam with SACLD treatment are modeled by disregarding the gap of the cutout and placing the cutout at the node between the elements. Section 3.1 validates the ACLD/SACLD model for different treatments. Section 3.2 verifies the effectiveness of the segmentation method's vibration suppression by performing a dynamic response analysis of the SACLD rotating beam. The effects of the control gains, the viscoelastic damping-layer thickness, the hub radius, and the beam width on the vibration are discussed. Section 3.3 discusses the modal analysis of the structure concerning natural frequencies and damping ratios. The effects of the relevant parameters on the modal state of the SACLD rotating beam are investigated. The research in this paper provides a new dynamical model for active and passive hybrid vibration control of flexible beam structures undergoing large overall rotational motion.

## 2. Dynamic Modeling

### *2.1. Basic Assumptions*

The rotating flexible beam with segmented active constrained layer damping treatment meets the following six assumptions:

(1) The SACLD beam consists of three layers, a piezoelectric constraining layer, a viscoelastic damping layer, and a base layer, without considering the sliding between the layers;
(2) The shear displacement of the piezoelectric and base layers is neglected; only the shear displacement of the viscoelastic damping layer is considered;
(3) The piezoelectric layer is polarized along the thickness direction;
(4) The longitudinal contraction caused by transversal displacement is considered for each beam;
(5) The beam rotates on a horizontal plane, without considering the effect of gravity;
(6) The transverse displacements of the three layers are considered the same.

### *2.2. Displacement Description*

Unlike the cantilever beams studied in Ref. [55], this paper considers the rotation of the beam and studies the flexible beam with a fully covered SACLD treatment. Figure 1 shows a schematic diagram of the overall structure of a flexible beam with a SACLD treatment attached to a rigid hub. The center rigid body rotates around the $Y$-axis. In this study, the gap between the cuts is ignored. Figure 2 shows a displacement description of the rotating SACLD beam; $u_1$, $u_2$, and $u_3$ are the displacements in $X$ axis of the base layer, the viscoelastic damping layer, and the piezoelectric constraining layer, respectively; $h_1$, $h_2$, and $h_3$ are the thicknesses of the base layer, the viscoelastic damping layer, and the piezoelectric constraining layer, respectively; and $\theta$ is the angle of rotation of the beam. The displacements of the upper and lower ends of the left end of the viscoelastic layer on the $X$ axis are represented by $u_A$ and $u_B$, respectively:

$$\begin{cases} u_A = u_1 - \dfrac{h_1}{2} \cdot \dfrac{\partial w}{\partial x} \\ u_B = u_3 + \dfrac{h_3}{2} \cdot \dfrac{\partial w}{\partial x} \end{cases} \tag{1}$$

where $w$ is the transverse displacement of the layers of the beam. The shear strain in the viscoelastic layer can be expressed as:

$$\gamma = \frac{u_3 - u_1 + dw'}{h_2} \tag{2}$$

where $d = \frac{h_1+2h_2+h_3}{2}$, and a prime denotes a derivative with respect to the argument.

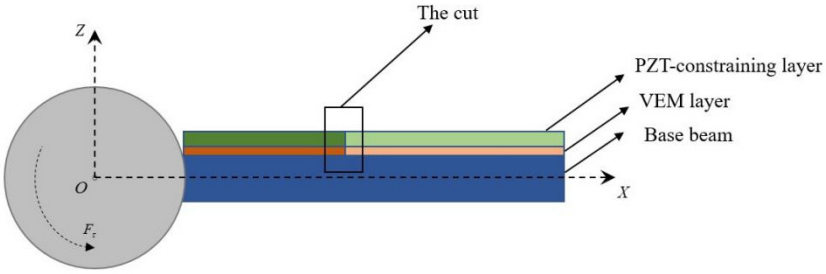


**Figure 1.** Schematic diagram of the rotating flexible beam with SACLD treatment attached to a rigid hub.

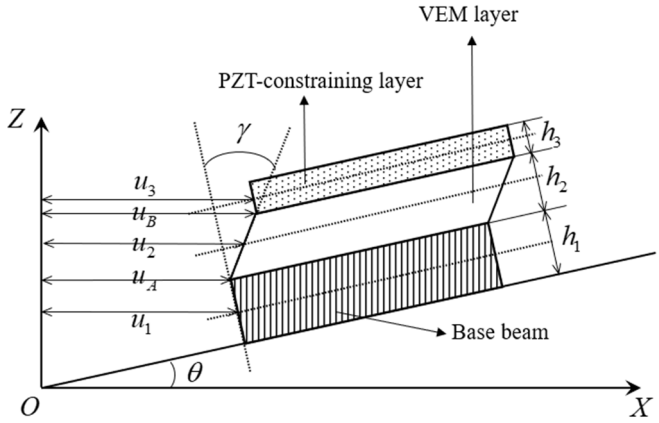


**Figure 2.** Displacement description of the beam with SACLD treatment.

Based on the geometric relationship shown in Figure 2, $u_2$ can be derived as:

$$u_2 = \frac{1}{2}(u_A + u_B) = \frac{1}{2}(u_1 + u_3 + d_1 w') \tag{3}$$

where $d_1 = \frac{h_3 - h_1}{2}$.

The position vector of an arbitrary point on the composite beam in the plane coordinate system *O*-*XZ* can be expressed as:

$$\boldsymbol{r}_i = (R + x + u_i)\boldsymbol{x} + w\boldsymbol{z}\ ,\ i = 1, 2, 3 \tag{4}$$

where $R$ is the radius of the hub. $u_i$ can be expressed as:

$$u_i = w_i + w_c \tag{5}$$

where $w_i$ indicates the displacement of each layer along its neutral axis; $w_c$ represents the axial shortening displacement caused by the transverse bending of the beam, which can be written as a second-order coupling term:

$$w_c = -\frac{1}{2}\int_0^x \left(\frac{\partial w(\xi,\ t)}{\partial \xi}\right)^2 \mathrm{d}\xi \tag{6}$$

*2.3. Kinetic Energy and Potential Energy*

For a SACLD beam rotating around a fixed axis, the kinetic energy can be expressed as:

$$\begin{aligned} T = &\ \tfrac{1}{2} J_{oh}\dot{\theta}^2 + \tfrac{1}{2}\sum_{i=1}^{3}\int_0^L \rho_i A_i \dot{\boldsymbol{r}}_i^{\mathrm{T}}\dot{\boldsymbol{r}}_i \mathrm{d}x \\ = &\ \tfrac{1}{2} J_{oh}\dot{\theta}^2 + \tfrac{1}{2}\sum_{i=1}^{3}\rho_i A_i \int_0^L \left\{ \left[(R + x + u_i)\dot{\theta} + \dot{w}\right]^2 + \left(\dot{u}_i - \dot{\theta} w\right)^2 \right\} \mathrm{d}x \end{aligned} \tag{7}$$

where $J_{oh}$ is the rotary inertia of the central hub; $\dot{\theta}$ is the angular velocity; and $A_1$, $A_2$, and $A_3$ are the cross-sectional areas of the three layers, respectively.

The potential energy of the system can be described as $U = U_1 + U_2 + U_3$, where $U_1$, $U_2$, and $U_3$ represent the potential energy of the piezoelectric, viscoelastic, and base beam layers, respectively.

The potential energy of the base beam layer can be expressed as:

$$U_1 = \frac{1}{2}\int_0^L \left[E_1 A_1 {u_1}'^2 + E_1 I_1 w''^2\right] \mathrm{d}x \tag{8}$$

The shear-strain energy of the viscoelastic layer can be represented as:

$$U_{shear} = \frac{1}{2} G^* A_2 \int_0^L \gamma^2 \mathrm{d}x \tag{9}$$

The total potential energy of the viscoelastic layer is:

$$U_2 = \frac{1}{2} G^* A_2 \int_0^L \gamma^2 \mathrm{d}x + \frac{1}{2} \int_0^L \left[ E_2 A_2 {u_2}'^2 + E_2 I_2 w''^2 \right] \mathrm{d}x \tag{10}$$

Piezoelectric material is assumed to be isotropic and is polarized along the thickness direction. The one-dimensional constitutive equations of the piezoelectric material are:

$$\begin{cases} \sigma_x^p = E_3 \varepsilon_x^p - e_{31} E_Z = E_3 \left( \dfrac{\partial w_3}{\partial x} - z \dfrac{\partial^2 w}{\partial x^2} \right) - e_{31} E_Z \\ D_Z = e_{31} \varepsilon_x^p + \in_{33} E_Z = e_{31} \left( \dfrac{\partial w_3}{\partial x} - z \dfrac{\partial^2 w}{\partial x^2} \right) + \in_{33} E_Z \end{cases} \tag{11}$$

where $\sigma_x^p$ and $\varepsilon_x^p$ denote the axial stress and strain of the piezoelectric layer, respectively; $E_3$ is the elastic modulus of the piezoelectric layer; $e_{31}$ represents the piezoelectric stress constant; $\in_{33}$ denotes the dielectric constant; and $E_Z$ and $D_Z$ denote the electric field and electric displacement of the piezoelectric layer along the polarization direction, respectively. Based on the above description, the potential energy of the piezoelectric layer can be expressed as:

$$U_3 = \iiint \sigma_x^p \varepsilon_x^p \mathrm{d}V = \frac{1}{2} \int_0^L \left[ E_3 A_3 {u_1'}^2 + E_3 I_3 w''^2 - 2 A_3 e_{31} E_Z {u_3}' - A_3 \in_{33} {E_Z}^2 \right] \mathrm{d}x \tag{12}$$

In this paper, the finite element method is carried out to discretize the SACLD beam. Figure 3 shows the schematic diagram of the finite element model of the beam, which is divided into $n_e$ elements, and the length of the $e$-th element is $L_e$. Figure 4 shows the schematic illustration of the $e$-th element of the beam. The distance between the origins of the element–coordinate system $\overline{o} - \overline{xz}$ and the floating coordinate system $\overline{O} - \overline{XZ}$ is represented by $x_e$; $\overline{x}$ is the longitudinal coordinate of an arbitrary point under the element–coordinate system. The spatial distribution corresponding to $w_1$, $w_2$, and $w_3$ of the $e$-th element is:

$$\begin{cases} w_1 = a_1 \overline{x} + a_2 \\ w_3 = a_3 \overline{x} + a_4 \\ w = a_5 \overline{x}^3 + a_6 \overline{x}^2 + a_7 \overline{x} + a_8 \end{cases} \tag{13}$$

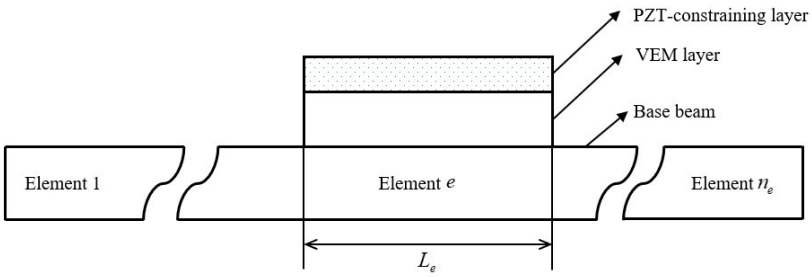


**Figure 3.** The finite element model of the SACLD beam.

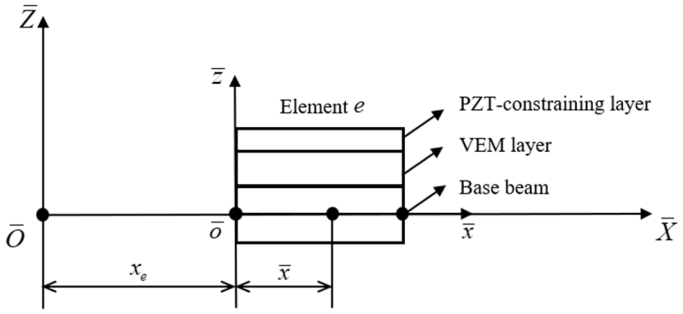


**Figure 4.** Illustration of the $e$-th element.

The nodal displacement vector for the $e$-th element is:

$$\boldsymbol{q}_e = \left\{ w_{1j}\ w_{3j}\ w_j\ w_j'\ w_{1k}\ w_{3k}\ w_k\ w_k' \right\}^{\mathrm{T}} \tag{14}$$

The element displacement vector is related to the node displacement vector by:

$$\begin{cases} w_1 = \boldsymbol{N}_1 \cdot \boldsymbol{q}_e \\ w_2 = \boldsymbol{N}_2 \cdot \boldsymbol{q}_e \\ w_3 = \boldsymbol{N}_3 \cdot \boldsymbol{q}_e \\ w = \boldsymbol{N}_4 \cdot \boldsymbol{q}_e \\ w' = \boldsymbol{N}_5 \cdot \boldsymbol{q}_e \\ \gamma = \boldsymbol{N}_6 \cdot \boldsymbol{q}_e \end{cases} \tag{15}$$

where $\boldsymbol{N}_1$, $\boldsymbol{N}_2$, $\boldsymbol{N}_3$, $\boldsymbol{N}_4$, $\boldsymbol{N}_5$, and $\boldsymbol{N}_6$ are the corresponding finite element shape functions of $w_1$, $w_2$, $w_3$, $w$, $w'$, and $\gamma$, respectively:

$$\begin{cases} \boldsymbol{N}_1 = \left[ \begin{array}{cccccccc} 1-\xi & 0 & 0 & 0 & \xi & 0 & 0 & 0 \end{array} \right] \\ \boldsymbol{N}_2 = \frac{1}{2}(\boldsymbol{N}_1 + \boldsymbol{N}_3 + d_1 \boldsymbol{N}_4') \\ \boldsymbol{N}_3 = \left[ \begin{array}{cccccccc} 0 & 1-\xi & 0 & 0 & 0 & \xi & 0 & 0 \end{array} \right] \\ \boldsymbol{N}_4 = \left[ \begin{array}{cccccccc} 0 & 0 & 1-3\xi^2+2\xi^3 & \left(\xi - 2\xi^2 + \xi^3\right) L_e & 0 & 0 & 3\xi^2 - 2\xi^3 & \left(-\xi^2 + \xi^3\right) L_e \end{array} \right] \\ \boldsymbol{N}_5 = \boldsymbol{N}_4' \\ \boldsymbol{N}_6 = \frac{1}{h_2}(\boldsymbol{N}_3 - \boldsymbol{N}_1 + d\boldsymbol{N}_4') \end{cases} \tag{16}$$

where $\xi = \frac{\bar{x}}{L_e}$. Thus, the overall nodal displacement vector of the beam can be obtained as:

$$\boldsymbol{q} = \left\{ w_1^{(1)}\ \ w_3^{(1)}\ \ w^{(1)}\ \ w'^{(1)}\ \ \cdots\ \ w_1^{(n+1)}\ \ w_3^{(n+1)}\ \ w^{(n+1)}\ \ w'^{(n+1)} \right\}^{\mathrm{T}} \tag{17}$$

The nonlinear coupled displacements $w_c$ are obtained under finite element discretization:

$$w_C = -\frac{1}{2}\boldsymbol{q}^{\mathrm{T}} \boldsymbol{S}(e, \bar{x}) \boldsymbol{q} \tag{18}$$

where

$$\boldsymbol{S}(e, \bar{x}) = \boldsymbol{B}_e^{\mathrm{T}} \int_0^{\bar{x}} \left( \frac{\partial \boldsymbol{N}_4}{\partial \bar{x}} \right)^{\mathrm{T}} \left( \frac{\partial \boldsymbol{N}_4}{\partial \bar{x}} \right) \mathrm{d}\bar{x} \boldsymbol{B}_e + \sum_{j=1}^{e-1} \left\{ \boldsymbol{B}_j^{\mathrm{T}} \int_0^{L_j} \left( \frac{\partial \boldsymbol{N}_4}{\partial \bar{x}} \right)^{\mathrm{T}} \left( \frac{\partial \boldsymbol{N}_4}{\partial \bar{x}} \right) \mathrm{d}\bar{x} \boldsymbol{B}_j \right\} \tag{19}$$

$$\boldsymbol{B}_e = \begin{bmatrix} 0 & 0 & \cdots & \boldsymbol{I}_4 & 0 & \cdots & 0 \\ 0 & 0 & \cdots & 0 & \boldsymbol{I}_4 & \cdots & 0 \end{bmatrix} \in \mathrm{R}^{8 \times 4(n_e+1)} \tag{20}$$

Substituting Equations (14), (15) and (17) into Equation (5) yields the longitudinal displacement as well as the transverse displacement of each layer of each element as:

$$\begin{cases} {u_1}^{(e)} = \boldsymbol{N}_1\boldsymbol{q}_e - \dfrac{1}{2}\boldsymbol{q}^{\mathrm{T}}\boldsymbol{S}(e,\overline{x})\boldsymbol{q} \\ {u_2}^{(e)} = \boldsymbol{N}_2\boldsymbol{q}_e - \dfrac{1}{2}\boldsymbol{q}^{\mathrm{T}}\boldsymbol{S}(e,\overline{x})\boldsymbol{q} \\ {u_3}^{(e)} = \boldsymbol{N}_3\boldsymbol{q}_e - \dfrac{1}{2}\boldsymbol{q}^{\mathrm{T}}\boldsymbol{S}(e,\overline{x})\boldsymbol{q} \\ w^{(e)} = \boldsymbol{N}_4\boldsymbol{q}_e \end{cases} \tag{21}$$

Substituting Equation (21) into Equations (7)–(12) yields the kinetic and potential energies of the *e*-th finite of the beam:

$$\begin{aligned} T^{(e)} \quad &= \frac{1}{2}\dot{\theta}^2\int_0^{L_e}\Big[J_{oh} + \sum_{i=1}^{3} m_i(R+x_e+\overline{x})^2 + m_1\boldsymbol{q}_e^{\mathrm{T}}\boldsymbol{N}_1^{\mathrm{T}}\boldsymbol{N}_1\boldsymbol{q}_e + m_2\boldsymbol{q}_e^{\mathrm{T}}\boldsymbol{N}_2^{\mathrm{T}}\boldsymbol{N}_2\boldsymbol{q}_e \\ &+ m_3\boldsymbol{q}_e^{\mathrm{T}}\boldsymbol{N}_3^{\mathrm{T}}\boldsymbol{N}_3\boldsymbol{q}_e + \tfrac{1}{4}\sum_{i=1}^{3} m_i\boldsymbol{q}^{\mathrm{T}}\boldsymbol{S}\boldsymbol{q}\cdot\boldsymbol{q}^{\mathrm{T}}\boldsymbol{S}\boldsymbol{q} - \frac{1}{2}m_1\boldsymbol{q}^{\mathrm{T}}\boldsymbol{S}\boldsymbol{q}\cdot\boldsymbol{N}_1\boldsymbol{q}_e - \frac{1}{2}m_2\boldsymbol{q}^{\mathrm{T}}\boldsymbol{S}\boldsymbol{q}\cdot\boldsymbol{N}_2\boldsymbol{q}_e \\ &- \frac{1}{2}m_3\boldsymbol{q}^{\mathrm{T}}\boldsymbol{S}\boldsymbol{q}\cdot\boldsymbol{N}_3\boldsymbol{q}_e - \frac{1}{2}m_1\boldsymbol{q}_e^{\mathrm{T}}\boldsymbol{N}_1^{\mathrm{T}}\cdot\boldsymbol{q}^{\mathrm{T}}\boldsymbol{S}\boldsymbol{q} - \frac{1}{2}m_2\boldsymbol{q}_e^{\mathrm{T}}\boldsymbol{N}_2^{\mathrm{T}}\cdot\boldsymbol{q}^{\mathrm{T}}\boldsymbol{S}\boldsymbol{q} - \frac{1}{2}m_3\boldsymbol{q}_e^{\mathrm{T}}\boldsymbol{N}_3^{\mathrm{T}}\cdot\boldsymbol{q}^{\mathrm{T}}\boldsymbol{S}\boldsymbol{q} \\ &+ 2m_1(R+x_e+\overline{x})\boldsymbol{N}_1\boldsymbol{q}_e + 2m_2(R+x_e+\overline{x})\boldsymbol{N}_2\boldsymbol{q}_e + 2m_3(R+x_e+\overline{x})\boldsymbol{N}_3\boldsymbol{q}_e \\ &- \sum_{i=1}^{3} m_i(R+x_e+\overline{x})\boldsymbol{q}^{\mathrm{T}}\boldsymbol{S}\boldsymbol{q} + \sum_{i=1}^{3} m_i\boldsymbol{q}_e^{\mathrm{T}}\boldsymbol{N}_4^{\mathrm{T}}\boldsymbol{N}_4\boldsymbol{q}_e\Big]\mathrm{d}\overline{x} \\ &+ \dot{\theta}\int_0^{L_e}\Big[\sum_{i=1}^{3} m_i\,(R+x_e+\overline{x})\boldsymbol{N}_4\dot{\boldsymbol{q}}_e + m_1\boldsymbol{q}_e^{\mathrm{T}}\boldsymbol{N}_1^{\mathrm{T}}\boldsymbol{N}_4\dot{\boldsymbol{q}}_e - m_1\boldsymbol{q}_e^{\mathrm{T}}\boldsymbol{N}_4^{\mathrm{T}}\boldsymbol{N}_1\dot{\boldsymbol{q}}_e \\ &+ m_2\boldsymbol{q}_e^{\mathrm{T}}\boldsymbol{N}_2^{\mathrm{T}}\boldsymbol{N}_4\dot{\boldsymbol{q}}_e - m_2\boldsymbol{q}_e^{\mathrm{T}}\boldsymbol{N}_4^{\mathrm{T}}\boldsymbol{N}_2\dot{\boldsymbol{q}}_e - \frac{1}{2}\sum_{i=1}^{3} m_i\boldsymbol{q}^{\mathrm{T}}\boldsymbol{S}\boldsymbol{q}\cdot\boldsymbol{N}_4\dot{\boldsymbol{q}}_e + \sum_{i=1}^{3} m_i\boldsymbol{q}^{\mathrm{T}}\boldsymbol{S}\dot{\boldsymbol{q}}\cdot\boldsymbol{N}_4\boldsymbol{q}_e\Big]\mathrm{d}\overline{x} \\ &+ \frac{1}{2}\int_0^{L_e}\Big[m_1\dot{\boldsymbol{q}}_e^{\mathrm{T}}\boldsymbol{N}_1^{\mathrm{T}}\boldsymbol{N}_1\dot{\boldsymbol{q}}_e + m_2\dot{\boldsymbol{q}}_e^{\mathrm{T}}\boldsymbol{N}_2^{\mathrm{T}}\boldsymbol{N}_2\dot{\boldsymbol{q}}_e + m_3\dot{\boldsymbol{q}}_e^{\mathrm{T}}\boldsymbol{N}_3^{\mathrm{T}}\boldsymbol{N}_3\dot{\boldsymbol{q}}_e + \sum_{i=1}^{3} m_i\boldsymbol{q}^{\mathrm{T}}\boldsymbol{S}\dot{\boldsymbol{q}}\cdot\boldsymbol{q}^{\mathrm{T}}\boldsymbol{S}\dot{\boldsymbol{q}} \\ &- 2m_1\boldsymbol{q}^{\mathrm{T}}\boldsymbol{S}\dot{\boldsymbol{q}}\cdot\boldsymbol{N}_1\dot{\boldsymbol{q}}_e - 2m_2\boldsymbol{q}^{\mathrm{T}}\boldsymbol{S}\dot{\boldsymbol{q}}\cdot\boldsymbol{N}_2\dot{\boldsymbol{q}}_e - 2m_3\boldsymbol{q}^{\mathrm{T}}\boldsymbol{S}\dot{\boldsymbol{q}}\cdot\boldsymbol{N}_3\dot{\boldsymbol{q}}_e + \sum_{i=1}^{3} m_i\dot{\boldsymbol{q}}_e^{\mathrm{T}}\boldsymbol{N}_4^{\mathrm{T}}\boldsymbol{N}_4\dot{\boldsymbol{q}}_e\Big]\mathrm{d}\overline{x} \end{aligned} \tag{22}$$

$$\begin{aligned} U^{(e)} = \quad &\frac{1}{2}\sum_{i=1}^{3} E_iI_i\int_0^{L_e}\boldsymbol{q}_e^{\mathrm{T}}{\boldsymbol{N}_4''}^{\mathrm{T}}\boldsymbol{N}_4''\boldsymbol{q}_e\mathrm{d}\overline{x} + \frac{1}{2}E_1A_1\int_0^{L_e}\boldsymbol{q}_e^{\mathrm{T}}{\boldsymbol{N}_1'}^{\mathrm{T}}\boldsymbol{N}_1'\boldsymbol{q}_e\mathrm{d}\overline{x} \\ &+ \frac{1}{2}E_2A_2\int_0^{L_e}\boldsymbol{q}_e^{\mathrm{T}}{\boldsymbol{N}_2'}^{\mathrm{T}}\boldsymbol{N}_2'\boldsymbol{q}_e\mathrm{d}\overline{x} + \frac{1}{2}E_3A_3\int_0^{L_e}\boldsymbol{q}_e^{\mathrm{T}}{\boldsymbol{N}_3'}^{\mathrm{T}}\boldsymbol{N}_3'\boldsymbol{q}_e\mathrm{d}\overline{x} \\ &+ \frac{G^*A_2}{2}\int_0^{L_e}\boldsymbol{q}_e^{\mathrm{T}}{\boldsymbol{N}_6}^{\mathrm{T}}\boldsymbol{N}_6\boldsymbol{q}_e\mathrm{d}\overline{x} \end{aligned} \tag{23}$$

### *2.4. Equations of the System*

For closed-loop systems, the work done by the piezoelectric force and piezoelectric torque is:

$$W_p = \frac{1}{2}E_3A_3\int_0^{L_e}\left(\varepsilon_c\varepsilon_p + d\varepsilon_p w''\right)\mathrm{d}\overline{x} \tag{24}$$

where $\varepsilon_c = u_3'$ is the elastic axial strain in the piezoelectric layer; $\varepsilon_p = \dfrac{d_{31}\phi_c}{h_3}$ is the strain produced by the piezoelectric effect, in which $d_{31}$ indicates the piezoelectric strain constant. Regulating the control voltage $\phi_c$ with a proportional and derivative (PD) control law:

$$\phi_c = -K_p\phi_s - K_d\dot{\phi}_s \tag{25}$$

where $\phi_s = -\frac{{k_{31}}^2 D_d b}{g_{31} C} \int_0^{L_e} w'' \mathrm{d}\overline{x}$ is the sensor voltage, in which $C = 8.854 \times 10^{-12} \frac{A_s k_{3t}}{h_1}$; $A_s$ is the surface area of the sensor; $k_{3t}$ is the dielectric constant; $D_d = \frac{h_1}{2}$; $k_{31}$ denotes electromechanical coupling factor; and $g_{31}$ indicates the piezoelectric voltage coefficient. According to Equations (24) and (25), the discretized generalized piezoelectric force vector ${\boldsymbol{Q}_{pf}}^{(e)}$ and piezoelectric moment vector ${\boldsymbol{Q}_{pm}}^{(e)}$ are expressed as:

$$ {\boldsymbol{Q}_{pf}}^{(e)} = \left(K_p + K_d p\right) \begin{bmatrix} 0 & -1 & 0 & 0 & 0 & 1 & 0 & 0 \end{bmatrix}^{\mathrm{T}} \cdot \begin{bmatrix} 0 & 0 & 0 & -\frac{g}{2} & 0 & 0 & 0 & \frac{g}{2} \end{bmatrix} \boldsymbol{q}_e \tag{26} $$

$$ {\boldsymbol{Q}_{pm}}^{(e)} = \left(K_p + K_d p\right) \begin{bmatrix} 0 & 0 & 0 & -1 & 0 & 0 & 0 & 1 \end{bmatrix}^{\mathrm{T}} \cdot \begin{bmatrix} 0 & 0 & 0 & -\frac{gd}{2} & 0 & 0 & 0 & \frac{gd}{2} \end{bmatrix} \boldsymbol{q}_e \tag{27} $$

where $p = \frac{\mathrm{d}}{\mathrm{d}t}$, $g = \frac{E_3 b^2 d_{31} k_{31}^2 D_d}{g_{31} C}$. The generalized piezoelectric control force is ${\boldsymbol{Q}_p}^{(e)} = {\boldsymbol{Q}_{pf}}^{(e)} + {\boldsymbol{Q}_{pm}}^{(e)}$. The external driving force of the system is $F_\tau$. From the external driving force and the generalized piezoelectric control force, the generalized force can be obtained as:

$$ \boldsymbol{Q}^{(e)} = \begin{bmatrix} F_\tau \\ {\boldsymbol{Q}_p}^{(e)} \end{bmatrix} \tag{28} $$

Substituting the discrete kinetic energy, potential energy, and generalized force of the $e$-th element into Lagrange's equations of the second kind:

$$ \frac{\mathrm{d}}{\mathrm{d}t} \left( \frac{\partial T^{(e)}}{\partial \dot{\boldsymbol{q}}_e} \right) - \frac{\partial T^{(e)}}{\partial \boldsymbol{q}_e} + \frac{\partial U^{(e)}}{\partial \boldsymbol{q}_e} = \boldsymbol{Q}^{(e)} \tag{29} $$

yields the dynamical equations for the $e$-th element:

$$ \begin{bmatrix} {M_{11}}^{(e)} & {\boldsymbol{M}_{12}}^{(e)} \\ {\boldsymbol{M}_{21}}^{(e)} & {\boldsymbol{M}_{22}}^{(e)} \end{bmatrix} \begin{bmatrix} \ddot{\theta} \\ \ddot{\boldsymbol{q}} \end{bmatrix} = \begin{bmatrix} {Q_\theta}^{(e)} \\ {\boldsymbol{Q}_q}^{(e)} \end{bmatrix} \tag{30} $$

The mass matrix and generalized forces for the $e$-th element of Equation (30) are shown in Appendix A.

In this paper, notches are applied to the viscoelastic damping layer and the piezoelectric constraining layer of the beam as a means of segmentation. The cuts are placed at node $k$ between the two elements during the finite element modeling and are considered as discontinuities. As shown in Figure 5, the degree of freedom at the $k$-th node is changed from the original $\left\{ {w_1}^{(k)} \; {w_3}^{(k)} \; w^{(k)} \; {w'}^{(k)} \right\}$ to $\left\{ {w_1}^{(k)} \; {w_{3l}}^{(k)} \; {w_{3r}}^{(k)} \; w^{(k)} \; {w'}^{(k)} \right\}$, and the cutout is treated discontinuously during the element assembly. Integration of the mass matrix and generalized forces for the $e$-th element yields the equation of motion of SACLD in the global coordinate system as:

$$ \begin{bmatrix} M_{11} & \boldsymbol{M}_{12} \\ \boldsymbol{M}_{21} & \boldsymbol{M}_{22} \end{bmatrix} \begin{bmatrix} \ddot{\theta} \\ \ddot{\boldsymbol{q}} \end{bmatrix} = \begin{bmatrix} Q_\theta \\ \boldsymbol{Q}_q \end{bmatrix} \tag{31} $$

where $M_{11}$ denotes the rotational inertia of the SACLD beam. $\boldsymbol{M}_{12} = {\boldsymbol{M}_{21}}^{\mathrm{T}}$ is the nonlinear inertial coupling term between the rigid body motion and elastic displacement. $\boldsymbol{M}_{22}$ is the generalized mass array.

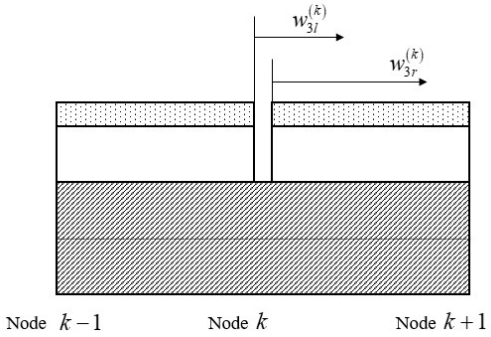


**Figure 5.** Illustration of the $k$th node.

It can be assumed that the angular velocity of the hub is constant at $\dot{\theta} = \Omega$, neglecting the higher order coupling terms in Equation (30) involving a nonlinear coupling term, and linearizing it to obtain the vibration equation for the $e$-th cell of the rotating SACLD beam as:

$$\widetilde{\boldsymbol{M}}_{22}{}^{(e)}\ddot{\boldsymbol{q}} + \widetilde{\boldsymbol{G}}_{22}{}^{(e)}\dot{\boldsymbol{q}} + \widetilde{\boldsymbol{K}}_{22}{}^{(e)}\boldsymbol{q} = \boldsymbol{0} \tag{32}$$

in which the generalized mass matrix $\widetilde{\boldsymbol{M}}_{22}{}^{(e)}$, the damping matrix $\widetilde{\boldsymbol{G}}_{22}{}^{(e)}$, and the element stiffness matrix $\widetilde{\boldsymbol{K}}_{22}{}^{(e)}$ are given in Appendix B.

The overall vibration equation of the system can be obtained by segmenting the beam during the finite element assembly as:

$$\widetilde{\boldsymbol{M}}_{22}\ddot{\boldsymbol{q}} + \widetilde{\boldsymbol{G}}_{22}\dot{\boldsymbol{q}} + \widetilde{\boldsymbol{K}}_{22}\boldsymbol{q} = \boldsymbol{0} \tag{33}$$

It should be noted that after applying $n$ cuts to the beam, the size of $\boldsymbol{q}$ changes from the previous $4(n_e+1)\times 1$ to $[4(n_e+1)+n]\times 1$. Correspondingly, the size of $\widetilde{\boldsymbol{M}}_{22}$, $\widetilde{\boldsymbol{G}}_{22}$, and $\widetilde{\boldsymbol{K}}_{22}$ will increase from $4(n_e+1)\times 4(n_e+1)$ to $[4(n_e+1)+n]\times[4(n_e+1)+n]$. And if the cuts number is 0, the model degrades into that of a rotating beam with ACLD treatment.

The vibration equation of the system is reduced in order and written in state space form:

$$\boldsymbol{A}\dot{\boldsymbol{z}} + \boldsymbol{B}\boldsymbol{z} = \boldsymbol{0} \tag{34}$$

where

$$\boldsymbol{z} = \begin{bmatrix} \dot{\boldsymbol{q}} \\ \boldsymbol{q} \end{bmatrix},\ \boldsymbol{A} = \begin{bmatrix} \widetilde{\boldsymbol{M}}_{22} & \boldsymbol{0} \\ \boldsymbol{0} & \boldsymbol{I} \end{bmatrix},\ \boldsymbol{B} = \begin{bmatrix} \widetilde{\boldsymbol{G}}_{22} & \widetilde{\boldsymbol{K}}_{22} \\ -\boldsymbol{I} & \boldsymbol{0} \end{bmatrix} \tag{35}$$

The eigenvalue problem associated with $\boldsymbol{A}\dot{\boldsymbol{z}} + \boldsymbol{B}\boldsymbol{z} = \boldsymbol{0}$ can be written as $(\lambda\boldsymbol{A} + \boldsymbol{B})\boldsymbol{\Theta} = \boldsymbol{0}$, in which $\boldsymbol{\Theta}_j$ denotes the corresponding complex eigenvector; $\lambda_j$ represents the vector of complex eigenvalues:

$$\lambda_j = \sigma_j + i\omega_j \tag{36}$$

where $\sigma_j$ indicates the vibration-index decay; $\omega_j$ denotes the $j$-th modal frequency. The loss factor of the $j$-th mode is:

$$\eta_j = -\frac{\sigma_j}{\sqrt{\sigma_j^2 + \omega_j^2}} \tag{37}$$

## 3. Results and Discussion

### *3.1. Validations of the Hub–SACLD Beam System*

In this section, three validation examples are used to verify the model. The first three modal frequencies are compared with the results from Ref. [12] (ACLD), Ref. [55] (SACLD), and the commercial software ANSYS (ACLD–SACLD) during the different rotating velocities and the base layer's relative thicknesses, respectively. Table 1 shows the comparison of the first three frequencies of the structure under different angular velocities between the hub–ACLD beam and this model. The comparison shows that the first three frequencies of the two models coincide very well, and the maximum error is 0.11%. Table 2

compares the first three frequencies with the base layer's relative thicknesses $H_b = \frac{h_1}{L}$ of 0.01, 0.012, and 0.015, respectively. The results indicate that the data are in good agreement with those of Ref. [55]. To further verify the accuracy of these models, it is necessary to validate the rotating ACLD and rotating SACLD beams. Table 3 compares the ACLD–SACLD model with the model established by ANSYS. The first three frequencies of the ACLD–SACLD rotating beam at angular velocities $\omega$ of 0–1000 rpm are compared. The two works are consistent with the data from each other. The above three validation examples show that this model is correct and can be used for analysis.

**Table 1.** Comparison between the model of Ref. [12] and the present model at different angular velocities (unit: Hz).

| $\omega$ (rpm) | Mode No. | Ref. [12] | Present | Err (%) |
|---|---|---|---|---|
| 200 | 1 | 20.21 | 20.21412 | 0.0253 |
| | 2 | 104.384 | 104.4093 | 0.0242 |
| | 3 | 277.427 | 277.4587 | 0.0114 |
| 600 | 1 | 20.5604 | 20.55981 | −0.0028 |
| | 2 | 106.685 | 106.7338 | 0.0457 |
| | 3 | 280.155 | 280.1561 | 0.11 |
| 1000 | 1 | 21.1927 | 21.19537 | 0.0126 |
| | 2 | 111.178 | 111.2351 | 0.0514 |
| | 3 | 285.44 | 285.466 | 0.0091 |

**Table 2.** The comparison of the cantilever SACLD beam model at different relative thicknesses of the base layer (unit: Hz).

| $H_b$ | Mode No. | Ref. [55] | Present | Err (%) |
|---|---|---|---|---|
| 0.01 | 1 | 18.9 | 19.4 | 2.6% |
| | 2 | 101 | 101.2 | 0.19% |
| | 3 | 283 | 283.8 | 0.28% |
| 0.012 | 1 | 21.5 | 21.9 | 1.8% |
| | 2 | 119 | 119.4 | 0.34% |
| | 3 | 334 | 334.8 | 0.24% |
| 0.015 | 1 | 25.6 | 25.9 | 1.17% |
| | 2 | 147 | 147.0 | 0.00% |
| | 3 | 412 | 412.4 | 0.97% |

**Table 3.** The comparison between the FEM model by ANSYS and the present model with ACLD–SACLD treatment at different angular velocities (unit: Hz).

| $\omega$ (rpm) | Mode No. | ACLD | | SACLD | |
|---|---|---|---|---|---|
| | | Present | ANSYS | Present | ANSYS |
| 0 | 1 | 20.16942 | 20.08 | 19.4 | 19.1 |
| | 2 | 104.1151 | 104.09 | 101.2 | 101.068 |
| | 3 | 277.1195 | 277.1 | 283.8 | 283.26 |
| 200 | 1 | 20.21412 | 20.261 | 19.47999 | 19.25 |
| | 2 | 104.4093 | 105.01 | 101.5351 | 101.451 |
| | 3 | 277.4587 | 277.96 | 284.176 | 283.76 |
| 600 | 1 | 20.55981 | 20.321 | 19.95035 | 20.047 |
| | 2 | 106.7338 | 106.3 | 103.8929 | 102.732 |
| | 3 | 280.1561 | 279.27 | 286.812 | 285.63 |
| 1000 | 1 | 21.19537 | 21.179 | 20.78848 | 20.665 |
| | 2 | 111.2351 | 111.201 | 108.4595 | 107.457 |
| | 3 | 285.466 | 286.2 | 292.0034 | 291.32 |

### 3.2. Dynamic Response Analysis

In this section, the dynamic response of the rotating SACLD beam is analyzed to verify the vibration-suppression effect. And the influences of control gains, viscoelastic layer thickness, central hub radius, and beam width on the dynamic response are discussed. The dynamics equations of the system Equation (31) are solved by the HHT-$\alpha$ method, which can be solved in small steps to reduce the dynamical equations' solution time and control the numerical damping's dissipation. Table 4 shows the physical parameters for the rotating SACLD beam. And the driving moment of the beam is set to:

$$F_\tau = \begin{cases} \tau_0 \sin\left(\dfrac{2\pi}{T}t\right), & 0 \le t \le T \\ 0, & t > T \end{cases} \tag{38}$$

where $\tau_0 = 1$ N·m, $T = 2$ s, and the simulation time is 3 s.

**Table 4.** Physical parameters of a rotating hub–beam system with SACLD treatment.

| Parameter | Value | Parameter | Value |
|---|---|---|---|
| $L$ | 0.3 m | $\rho_1$ | 2700 kg/m$^3$ |
| $L_e$ | 0.03 m | $\rho_2$ | 1250 kg/m$^3$ |
| $b$ | 0.0127 m | $\rho_3$ | 7600 kg/m$^3$ |
| $h_1$ | $1.8 \times 10^{-3}$ m | $G_2$ | $2 \times 10^6$ Pa |
| $h_2$ | $0.25 \times 10^{-3}$ m | $\eta$ | 0.38 |
| $h_3$ | $0.762 \times 10^{-3}$ m | $d_{31}$ | $23 \times 10^{-12}$ m/V |
| $E_1$ | 64.9 GPa | $g_{31}$ | 0.216 V·m/N |
| $E_2$ | $2(1+\eta)G^*$ | $k_{31}$ | 0.12 |
| $E_3$ | 64.9 Gpa | $k_{3t}$ | 12 |
| $X_k$ | 0.7 | $R$ | 0 |

Figure 6 compares the tip transverse displacement of the ACLD beam and the SACLD beam in an open-loop case. It can be seen that the segmentation method reduces the maximum transverse displacement amplitude of the rotating beam. The maximum transverse displacement amplitude of the rotating SACLD beam is also significantly smaller than the maximum vibration amplitude of the rotating ACLD beam at $t > T$, i.e., when the driving moment of the beam is zero. The vibration-suppression effect of SACLD is better than ACLD when the material parameters and dimensional parameters are given in Table 4.

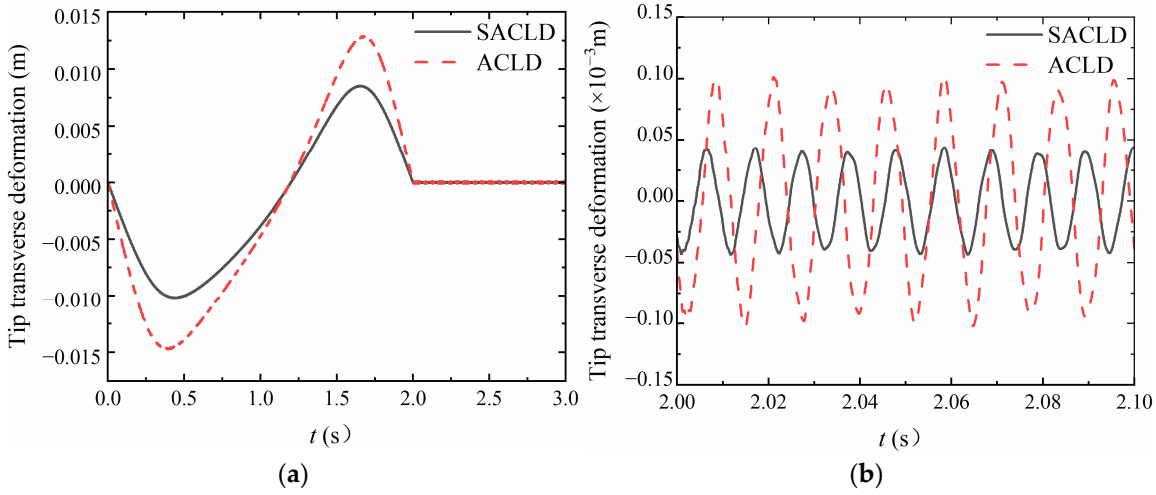


**Figure 6.** Tip transverse displacement of the ACLD–SACLD rotating beam in an open-loop case. (**a**) $0 < t < 3.0$ s; (**b**) 2.00 s $< t <$ 2.10 s.

Figure 7 shows the effect of the control gains on the transverse displacement of the SACLD rotating beam when $K_p = 1$, $K_d = -0.005$. It can be seen that the amplitude of the vibration of the SACLD beam becomes smaller and the vibration suppression of the beam is better when the control gains are applied to the SACLD beam. Therefore, the control for the vibration suppression is pronouncedly effective. Figure 8 shows the transverse displacement of the SACLD rotating beam for different proportional control coefficients $K_p$, while $K_d = 0$. It can be seen that the vibration-suppression effect of the SACLD rotating beam is better as the proportional control coefficient $K_p$ increases. The transverse displacement of the SACLD rotating beam decreases the most when $K_p = 5$. $K_p$ increases further on this basis; the transverse displacement of the structure also decreases, but the reduction is no longer obvious.

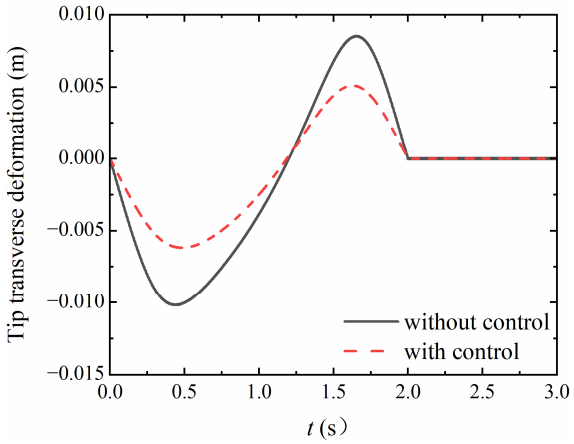


**Figure 7.** Comparison of the tip transverse displacements of the rotating SACLD beam.

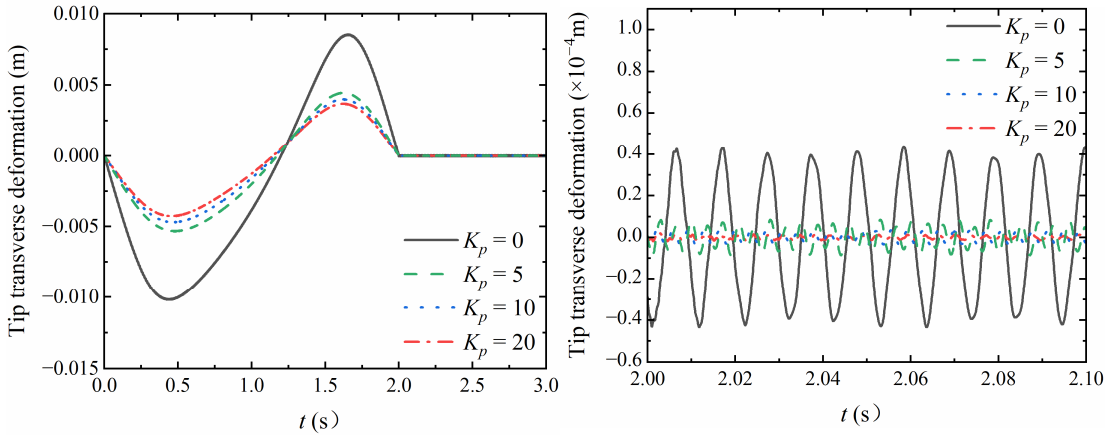


**Figure 8.** Transverse displacement of the rotating SACLD beam with different $K_p$. (**a**) $0 < t < 3.0$ s; (**b**) 2.00 s $< t <$ 2.10 s.

The effect of structural parameters on the dynamic response of the rotating SACLD beam is further analyzed. The rotating SACLD beam with different driving moments is used for dynamic analysis, and the driving moments of the SACLD rotating beam are set as:

$$F_\tau = 0.1\exp(-120t) \tag{39}$$

Figure 9 compares the effect of control on the dynamic response of the rotating SACLD beams when $K_p = 1$, $K_d = -0.005$. It can be seen that, applying control to the beam, the vibration amplitude of tip transverse displacement and longitudinal displacement of the beam are significantly reduced. Both the longitudinal displacement and transverse

displacement attenuate compared with the case without the control. Figure 10 compares the effect of $K_d$ on the dynamic response of the SACLD rotating beam. It can be seen that the tip displacement of the SACLD rotating beam decreases during the derivative control gain. $K_d$ is set to be $-0.01$ and $-0.005$, respectively, while the decreasing trend is faster when the gain is $-0.01$. Figure 11 compares the transverse and longitudinal displacement of the rotating SACLD beam when the VEM layer thickness is $h_2$ = 0.25 mm and 0.5 mm, respectively. It can be seen that, with the increase of the VEM layer thickness, the tip transverse displacement and tip longitudinal displacement of the SACLD beam are reduced, while the displacement amplitude reduction is more pronounced when the VEM layer thickness is larger. Figure 12 shows the dynamic response of the rotating SACLD beam with the central hub radius $R$ = 0 and 0.025 m, respectively. The results show that the tip transverse displacement and tip longitudinal displacement of the rotating SACLD beam increase after the radius of the central hub increases. And the displacement increase is due to the increase of the hub radius resulting in an increase in centrifugal force during the SACLD beam rotation. The radius of the central hub has less influence on the displacement of the end of the SACLD rotating beam. Figure 13 shows the effect of beam width $b$ on the dynamic response of the rotating SACLD beam. It can be seen that the tip transverse displacement and the tip longitudinal displacement of the SACLD rotating beam increase when the width of the beam decreases. And the width $b$ impacts the flexural rigidity and the tension rigidity of the beam; the decrease of the width makes the beam more flexible. The width of the beam has a more significant effect on the tip displacement of the SACLD rotating beam.

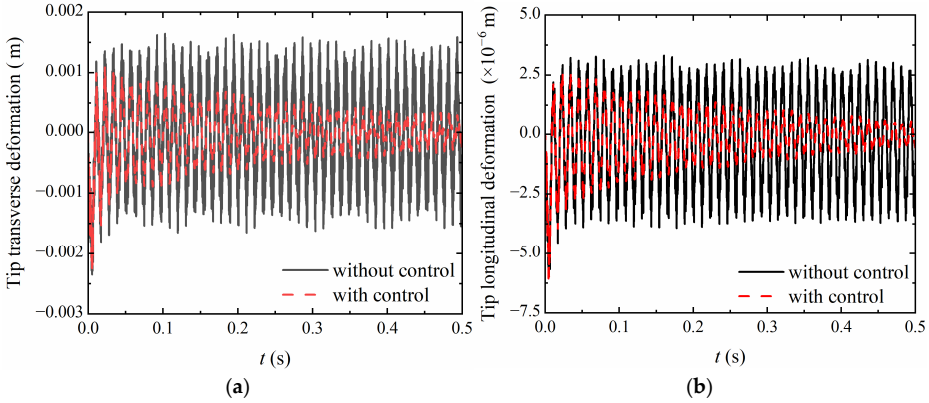


**Figure 9.** Effect of control on the dynamic response of the rotating SACLD beams: (**a**) tip transverse displacement of the beam; (**b**) tip longitudinal displacement of the beam.

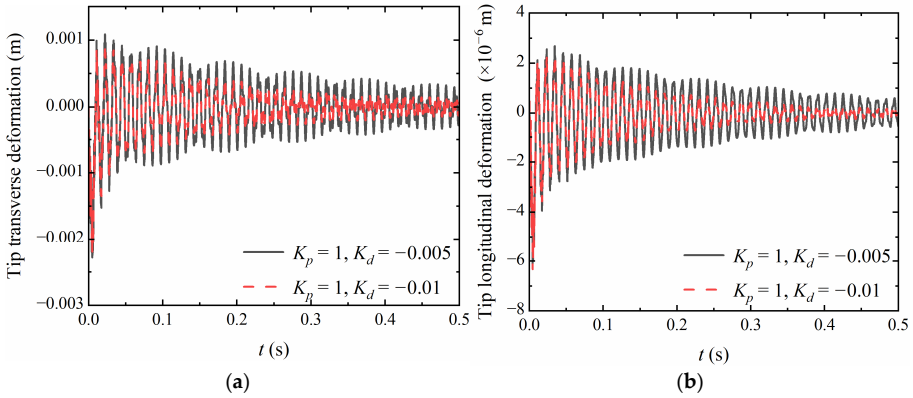


**Figure 10.** Effect of different control gains on the dynamic response of the rotating SACLD beams: (**a**) tip transverse displacement of the beam; (**b**) tip longitudinal displacement of the beam.

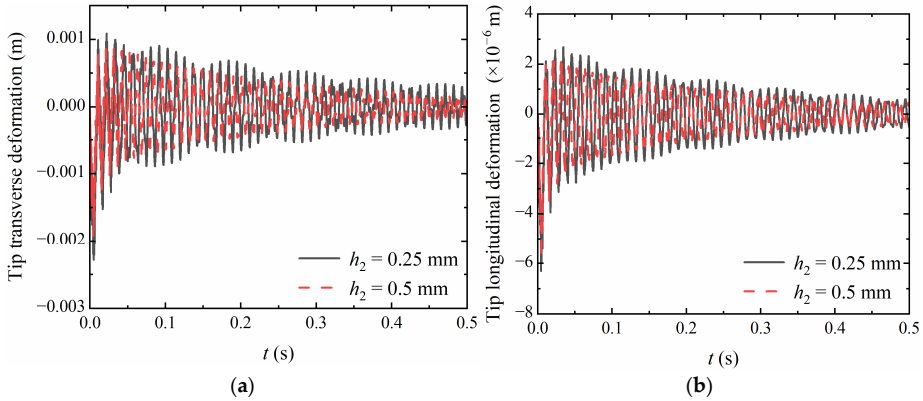


**Figure 11.** Effect of VEM layer thickness $h_2$ on the dynamic response of the rotating SACLD beams: (**a**) tip transverse displacement of the beam; (**b**) tip longitudinal displacement of the beam.

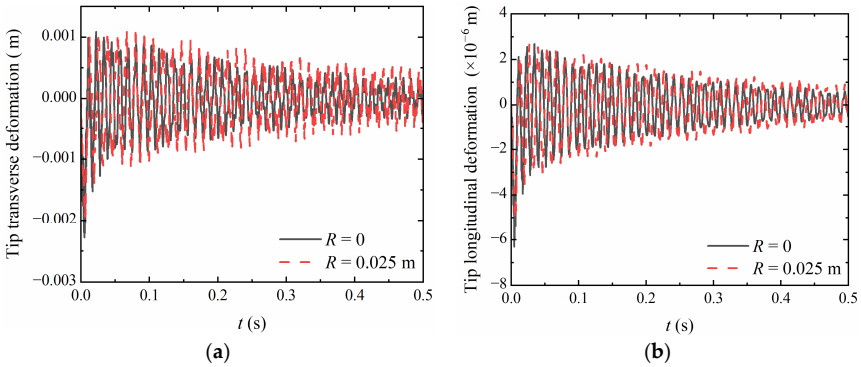


**Figure 12.** Effect of central rigid body radius $R$ on the dynamic response of the rotating SACLD beams: (**a**) tip transverse displacement of the beam; (**b**) tip longitudinal displacement of the beam.

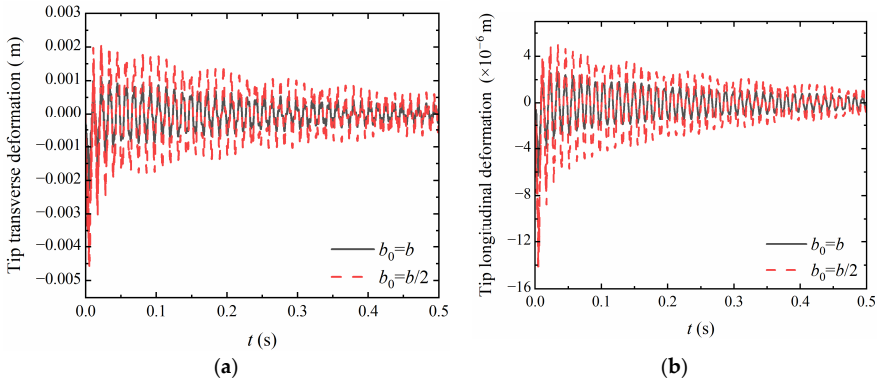


**Figure 13.** Effect of beam width $b$ on the dynamic response of the rotating SACLD beams: (**a**) tip transverse displacement of the beam; (**b**) tip longitudinal displacement of the beam.

### *3.3. Vibration Analysis*

This section performs a modal vibration analysis of the flexible hub–beam covered with SACLD treatment. The physical parameters of the SACLD rotating beam are the same as those given in Table 4. Since segmentation is not always effective [55], and the level of shear strain inside the viscoelastic material layer affects the applicability and effectiveness of the segmentation, it is necessary to investigate the effect of the relative thicknesses of the base beam, the PZT layer, and the VEM layer on the structural vibration.

The following size ratios are defined for a broad comparison of the findings. The dimensionless ratio parameters are used to describe the relative thicknesses of the layers as well as the location of the cuts:

$$H_b = \frac{h_1}{L},\ H_v = \frac{h_2}{h_1},\ H_c = \frac{h_3}{L},\ 0 < X_k < 1 \tag{40}$$

where $H_b$, $H_v$, and $H_c$ are the relative thicknesses of the base layer, VEM layer, and PZT layer, respectively. $X_k$ is the location of the cutout.

Figures 14–16 show the variation of the first three natural frequencies and damping ratios with the relative thickness of the VEM layer for the ACLD beam (the cuts number is 0), and SACLD beams with the numbers of cuts of one, two, and three, with $H_b = H_c$ of 0.001, 0.005, and 0.012 when the angular velocity $\omega = 0$, $K_p = 0$, and $K_d = 0$. According to the study of Tian et al. [55], the notch position of one notch is set as $X_k = 0.7$. Set the notch positions for two cutouts to $X_{k1} = 0.3$ and $X_{k2} = 0.7$, and for the case of three notches, set the notch positions to $X_{k1} = 0.3$, $X_{k2} = 0.4$, and $X_{k3} = 0.7$ according to Mohammed's optimal design of the notch positions [52]. It can be seen in Figure 14 that the segmentation method consistently reduces the first three frequencies of the beam when $H_b = H_c = 0.001$. The reduction effect on the first three frequencies is always greater for three cuts than for two cuts, and one cut has the relatively smallest reduction on the first three frequencies. The segmentation method can always increase the first three damping ratios when $H_b = H_c = 0.001$. The enhancement effect on the first three damping ratios is always the best with three cuts, followed by two cuts, and the worst with one cut. It can be shown that the SACLD beam has a better damping effect than the ACLD beam when $H_b = H_c = 0.001$. With the increased number of cuts, the vibration-damping effect of the segmental method is better when $H_b = H_c = 0.001$. It can be seen from Figure 15 that the segmentation method consistently reduces the first three frequencies when $H_b = H_c = 0.005$. As the number of cuts increases, the segmentation method is more effective in reducing the first three frequencies of the beam. However, the segmentation method does not always reduce the first three damping ratios, with the base layer's relative thickness and the PZT layer's relative thickness becoming thicker. The segmentation method can improve the first-order damping ratio when $H_b = H_c = 0.005$. The best vibration-suppression effect is achieved at the two cuts. However, as the VEM layer's relative thickness increases, the damping effect of three cuts changes from better than that of one cut to worse than that of one cut. With the increase of the VEM layer's relative thickness, the second-order damping ratio is smaller than that of the ACLD beam. At this time, the damping effect of one cut is the best, followed by two cuts, and that of three cuts is the worst. For the third-order damping ratio, with the increase of the VEM layer's relative thickness, the third-order damping ratio of the SACLD beam is smaller than that of the ACLD beam. It can be seen from Figure 16 that the segmentation method always reduces the first three frequencies when $H_b = H_c = 0.012$. Applying one cut to the ACLD beam can always increase the first-order damping ratio. However, only when the VEM layer's relative thickness is small, applying two notches and three notches can improve the first-order damping ratio. In this case, the segmentation method cannot increase the second-order and third-order damping ratios. A comparative analysis of Figures 14–16 shows that the segmentation method can always reduce the first three frequencies when $H_b = H_c = 0.001$–$0.012$. However, the vibration-suppression effect of the segmentation method gradually becomes smaller as the relative thickness of the base layer and the PZT layer increases. It can be shown that, with the increase of the base layer's relative thickness and the PZT layer's thickness, the shear-strain level within the VEM layer increases, and the segmentation method changes from effective to ineffective.

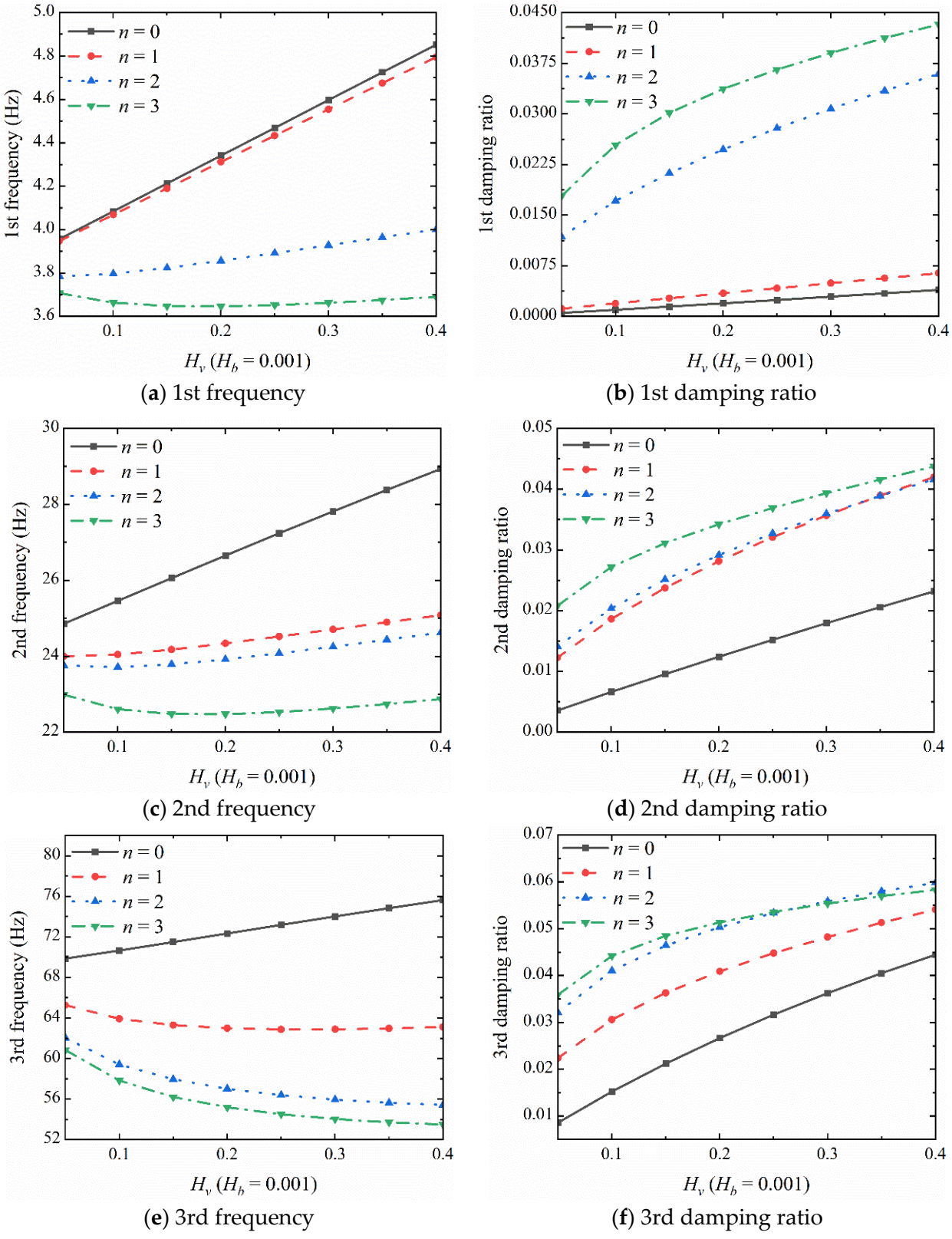


**Figure 14.** Variations of the first three natural frequencies and damping ratios with the VEM layer's relative thickness when $H_b$ = 0.001.

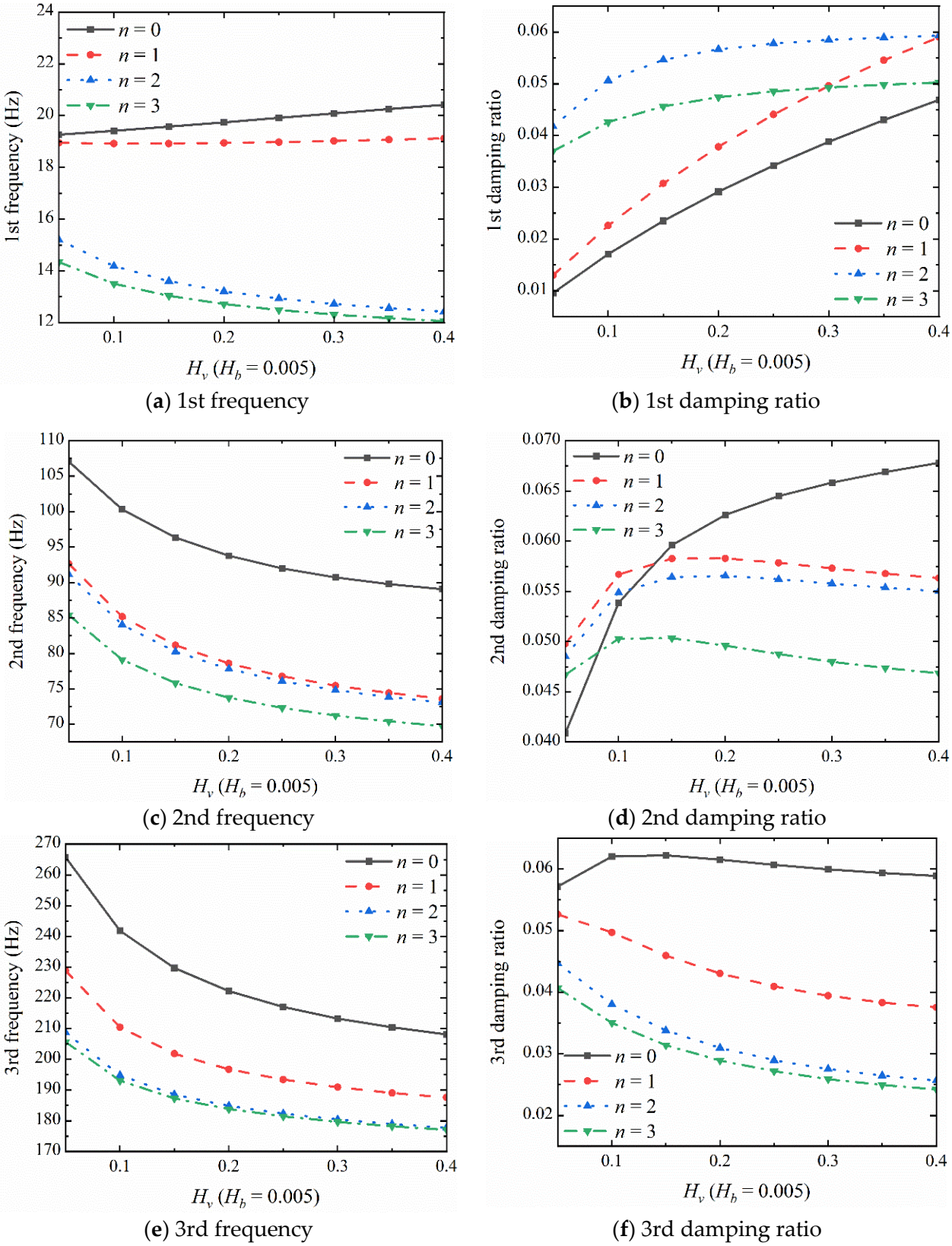


**Figure 15.** Variations of the first three natural frequencies and damping ratios with the VEM layer's relative thickness when $H_b$ = 0.005.

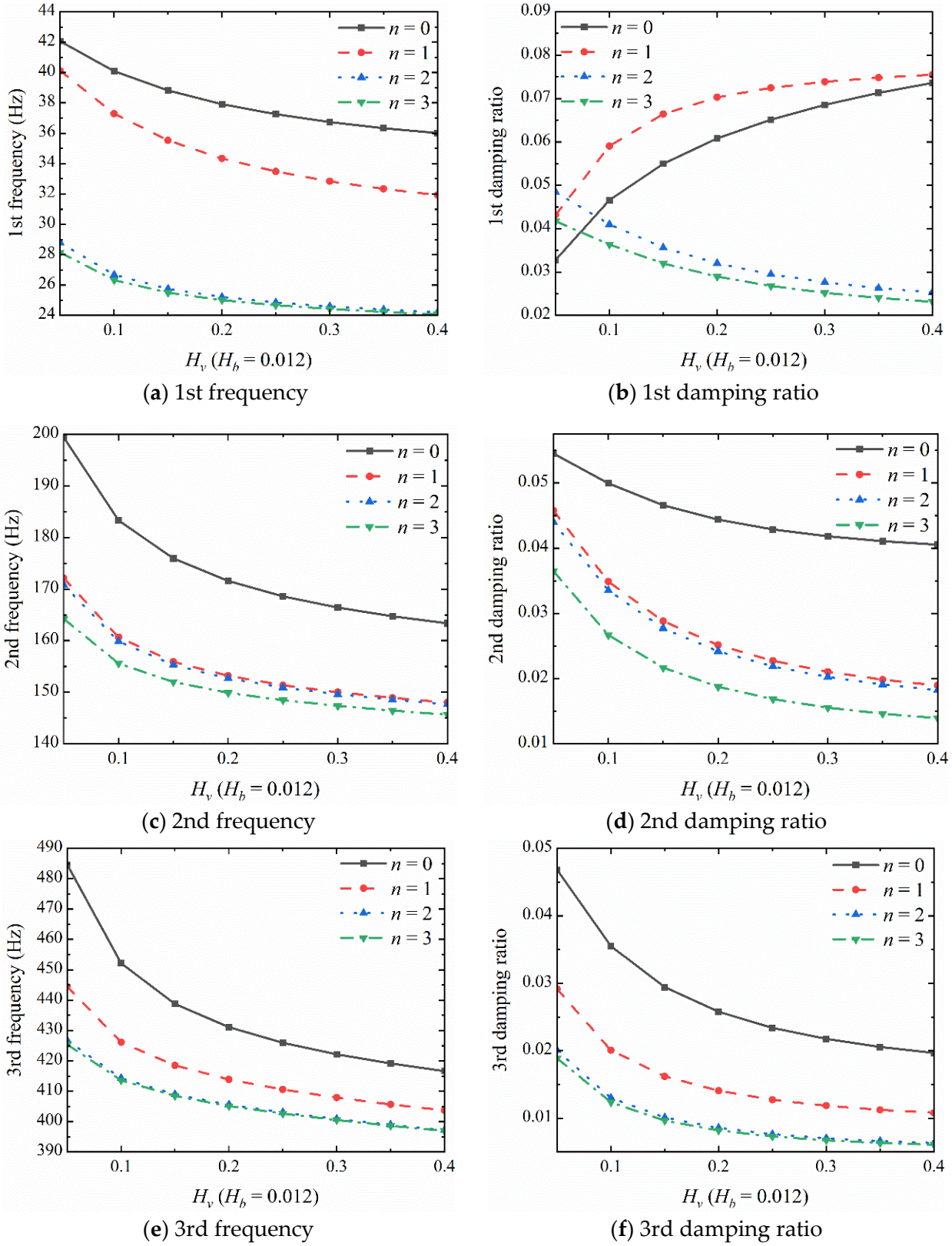


**Figure 16.** Variations of the first three natural frequencies and damping ratios with the VEM layer's relative thickness when $H_b$ = 0.012.

Figure 17 discusses the variation of the first three natural frequencies and damping ratios, with the angular velocity with the number of cuts of zero, one, two, and three, when $H_b = H_c = 0.012$, $H_v = 0.2$. It can be seen that the first three frequencies increase gradually with the increase of angular velocity. The segmentation method can reduce the first three natural frequencies. Only by applying one cut to the beam can the first damping ratio be increased. In this case, applying two and three notches to the beam reduces the first damping ratio. For the second-order and third-order damping ratios, the damping effect of three notches is the worst, followed by two notches, and the damping effect of one notch is relatively the best.

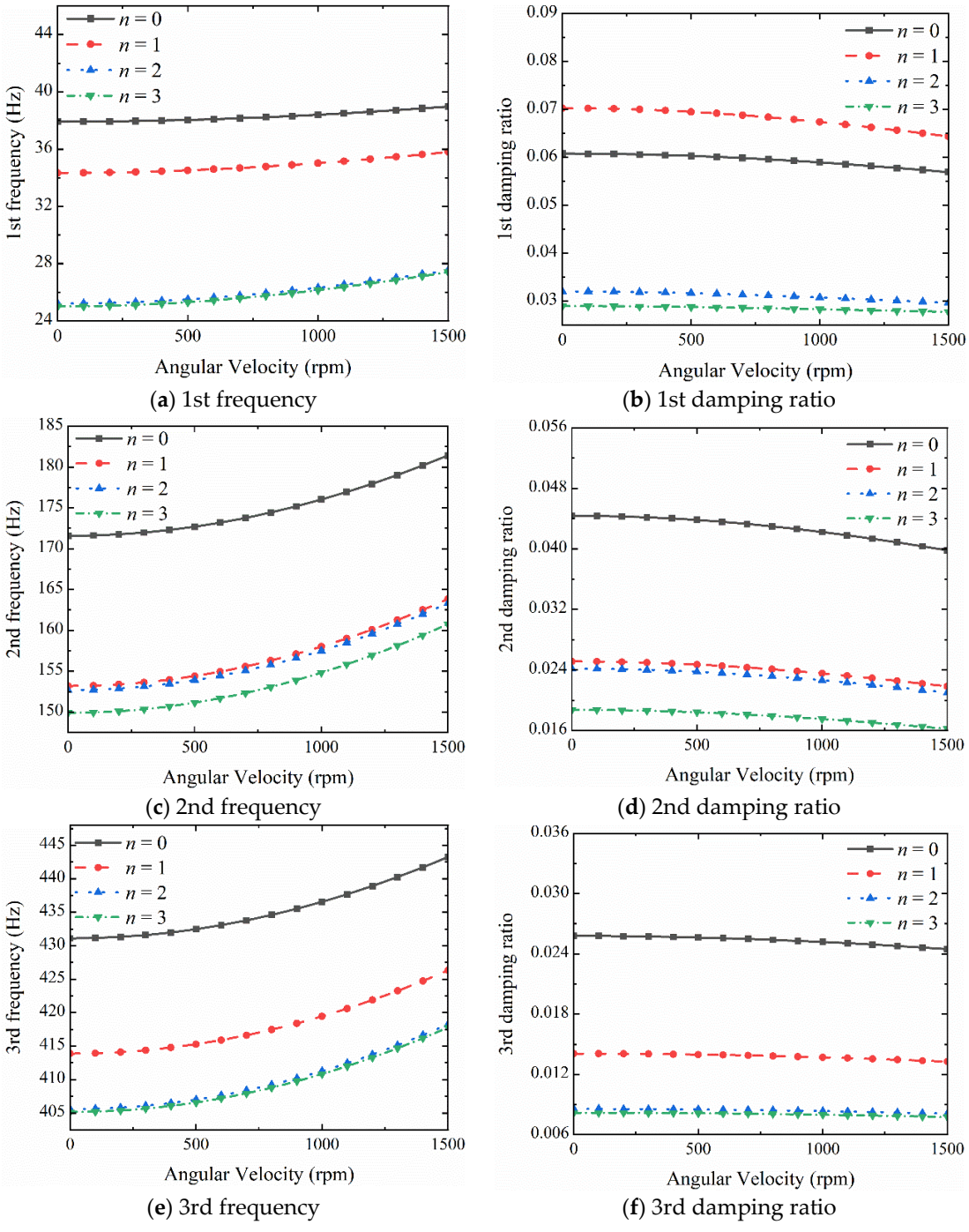


**Figure 17.** Variation of the first three frequencies and damping ratios with angular velocity.

Figure 18 shows the variation of the first three natural frequencies and damping ratios with the VEM layer loss factor $\eta$, with the number of cuts set to be zero, one, two, and three, respectively, when $H_b = H_c = 0.012$ and $H_v = 0.2$. It can be seen that the first three natural frequencies and damping ratios increase with the increase of $\eta$. While the natural frequencies and the damping ratios decrease with the increase of the cuts number, and the effect is obvious to the first and the third natural frequencies and damping ratio while the cut number is one and three, while the cut number is two, the vibration suppression is obvious to the second natural frequency and damping ratio.

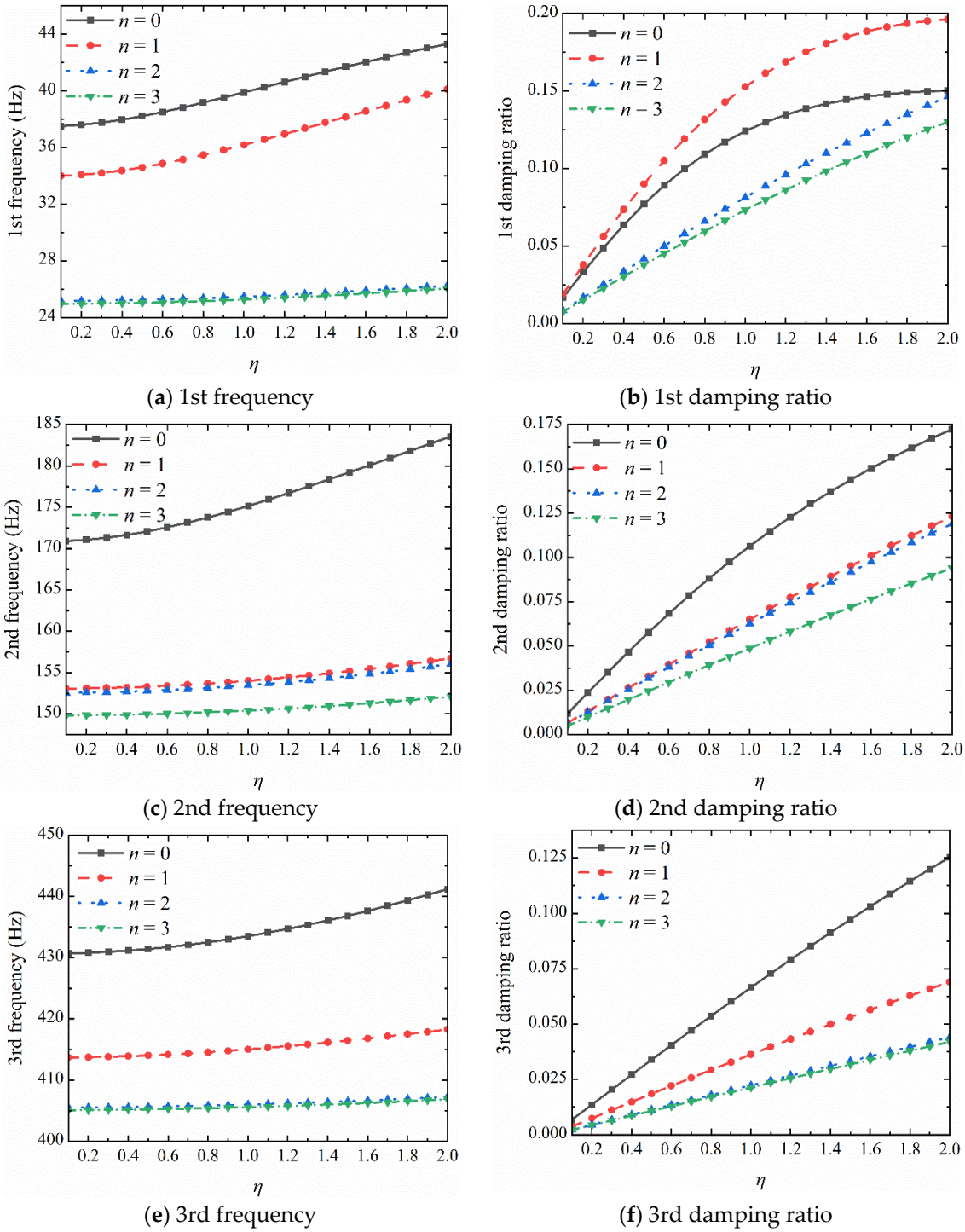


**Figure 18.** Variation of the first three natural frequencies and damping ratios with $\eta$.

Figures 19 and 20 discuss the active control of the first natural frequency and damping ratio by the proportional control gain $K_p$ of the PD control law with angular velocity in a closed-loop case when $n$ = 1 and $X_k$ = 0.7. It can be seen that the first natural frequency of the rotating SACLD beam decreases, and the first damping ratio increases as $K_p$ increases, which leads to the conclusion that the vibration-suppression effect of the rotating SACLD beam is better with $K_p$.

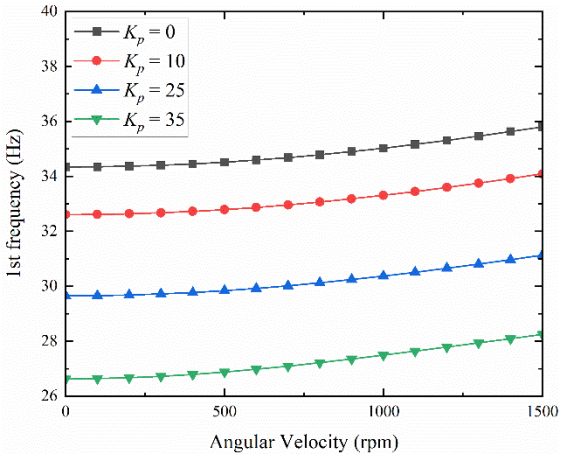


**Figure 19.** First natural frequency with angular velocity.

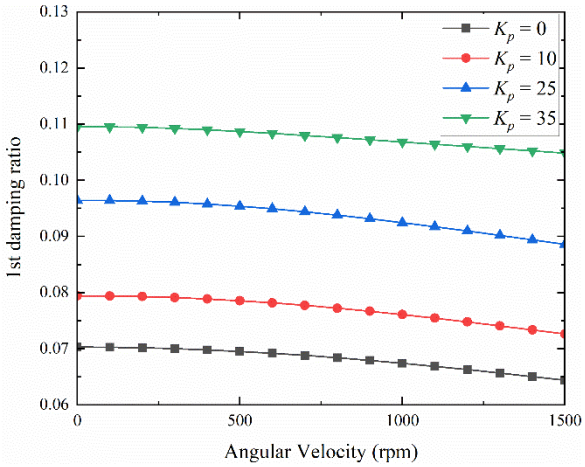


**Figure 20.** First damping ratio with angular velocity.

## 4. Conclusions

In this paper, based on the floating frame-of-reference method and finite element method, the dynamics of the hub–beam with a segmented active constrained layer damping treatment was modeled by disregarding the gap of the cutout and placing the cutout at the node between the elements. The discontinuity was set at the cutout location during finite element assembly. The dynamic response analysis of the SACLD beam shows that the segmental treatment of the ACLD beam had a better vibration-suppression effect when suitable material and dimensional parameters were used for it. The effects of control parameters, viscoelastic material layer thickness, central hub radius, and beam width on the dynamic response of the SACLD beam are discussed. Meanwhile, a modal vibration analysis of the SACLD beam was performed. It was found that the SACLD beam had better vibration suppression when compared with the ACLD beam when a smaller base beam thickness and piezoelectric constraining layer thickness were used. The vibration suppression of the SACLD beam could be improved by appropriately increasing the loss

factor of the viscoelastic damping layer and adopting appropriate control parameters. The research in this paper provided a new dynamical model for active and hybrid vibration control of flexible beam structures during large overall rotational motion.

**Author Contributions:** Conceptualization, L.L. and D.Z.; Methodology, Y.W.; Software, Y.F.; Validation, Y.W.; Writing—Original Draft Preparation, Y.W. and Y.F. Writing—Review and Editing, L.L. and W.-H.L.; Visualization, J.F. All authors have read and agreed to the published version of the manuscript.

**Funding:** This research was funded by grants from the National Natural Science Foundation of China (Project Nos. 12072159 and 12232012) and the Fundamental Research Funds for the Central Universities (Project No. 30922010314).

**Data Availability Statement:** The data presented in this study are available within the article.

**Conflicts of Interest:** The authors declare no conflict of interest.

## Appendix A. The Matrices in Equation (30)

$$\begin{aligned} M_{11}{}^{(e)} = \; & \int_0^{L_e}\Big[J_{oh}+\sum_{i=1}^{3} m_i(R+x_e+\overline{x})^2+m_1\boldsymbol{B}_e^{\mathrm{T}}\boldsymbol{q}_e{}^{\mathrm{T}}\boldsymbol{N}_1^{\mathrm{T}}\boldsymbol{N}_1\boldsymbol{q}_e\boldsymbol{B}_e+m_2\boldsymbol{B}_e^{\mathrm{T}}\boldsymbol{q}_e{}^{\mathrm{T}}\boldsymbol{N}_2^{\mathrm{T}}\boldsymbol{N}_2\boldsymbol{q}_e\boldsymbol{B}_e \\ & +m_3\boldsymbol{B}_e^{\mathrm{T}}\boldsymbol{q}_e{}^{\mathrm{T}}\boldsymbol{N}_3^{\mathrm{T}}\boldsymbol{N}_3\boldsymbol{q}_e\boldsymbol{B}_e+\frac{1}{4}\sum_{i=1}^{3} m_i\boldsymbol{q}^{\mathrm{T}}\boldsymbol{S}\boldsymbol{q}\cdot\boldsymbol{q}^{\mathrm{T}}\boldsymbol{S}\boldsymbol{q}-\frac{1}{2}m_1\boldsymbol{q}^{\mathrm{T}}\boldsymbol{S}\boldsymbol{q}\cdot\boldsymbol{N}_1\boldsymbol{q}_e\boldsymbol{B}_e \\ & -\frac{1}{2}m_2\boldsymbol{q}^{\mathrm{T}}\boldsymbol{S}\boldsymbol{q}\cdot\boldsymbol{N}_2\boldsymbol{q}_e\boldsymbol{B}_e-\frac{1}{2}m_3\boldsymbol{q}^{\mathrm{T}}\boldsymbol{S}\boldsymbol{q}\cdot\boldsymbol{N}_3\boldsymbol{q}_e\boldsymbol{B}_e-\frac{1}{2}m_1\boldsymbol{B}_e^{\mathrm{T}}\boldsymbol{q}_e{}^{\mathrm{T}}\boldsymbol{N}_1^{\mathrm{T}}\cdot\boldsymbol{q}^{\mathrm{T}}\boldsymbol{S}\boldsymbol{q} \\ & -\frac{1}{2}m_2\boldsymbol{B}_e^{\mathrm{T}}\boldsymbol{q}_e{}^{\mathrm{T}}\boldsymbol{N}_2^{\mathrm{T}}\cdot\boldsymbol{q}^{\mathrm{T}}\boldsymbol{S}\boldsymbol{q}-\frac{1}{2}m_3\boldsymbol{B}_e^{\mathrm{T}}\boldsymbol{q}_e{}^{\mathrm{T}}\boldsymbol{N}_3^{\mathrm{T}}\cdot\boldsymbol{q}^{\mathrm{T}}\boldsymbol{S}\boldsymbol{q}+2m_1(R+x_e+\overline{x})\boldsymbol{N}_1\boldsymbol{q}_e\boldsymbol{B}_e \\ & +2m_2(R+x_e+\overline{x})\boldsymbol{N}_2\boldsymbol{q}_e\boldsymbol{B}_e+2m_3(R+x_e+\overline{x})\boldsymbol{N}_3\boldsymbol{q}_e\boldsymbol{B}_e \\ & -\sum_{i=1}^{3} m_i(R+x_e+\overline{x})\boldsymbol{q}^{\mathrm{T}}\boldsymbol{S}\boldsymbol{q}+\sum_{i=1}^{3} m_i\boldsymbol{B}_e^{\mathrm{T}}\boldsymbol{q}_e{}^{\mathrm{T}}\boldsymbol{N}_4^{\mathrm{T}}\boldsymbol{N}_4\boldsymbol{q}_e\boldsymbol{B}_e\Big]\mathrm{d}\overline{x} \end{aligned} \tag{A1}$$

$$\begin{aligned} \boldsymbol{M}_{12}{}^{(e)} = \; & \int_0^{L_e}\Big[\sum_{i=1}^{3} m_i(R+x_e+\overline{x})\boldsymbol{N}_4\boldsymbol{B}_e+m_1\boldsymbol{B}_e^{\mathrm{T}}\boldsymbol{q}_e{}^{\mathrm{T}}\boldsymbol{N}_1^{\mathrm{T}}\boldsymbol{N}_4-m_1\boldsymbol{B}_e^{\mathrm{T}}\boldsymbol{q}_e{}^{\mathrm{T}}\boldsymbol{N}_4^{\mathrm{T}}\boldsymbol{N}_1 \\ & +m_2\boldsymbol{B}_e^{\mathrm{T}}\boldsymbol{q}_e{}^{\mathrm{T}}\boldsymbol{N}_2^{\mathrm{T}}\boldsymbol{N}_4-m_2\boldsymbol{B}_e^{\mathrm{T}}\boldsymbol{q}_e{}^{\mathrm{T}}\boldsymbol{N}_4^{\mathrm{T}}\boldsymbol{N}_2+m_3\boldsymbol{B}_e^{\mathrm{T}}\boldsymbol{q}_e{}^{\mathrm{T}}\boldsymbol{N}_3^{\mathrm{T}}\boldsymbol{N}_4 \\ & -m_3\boldsymbol{B}_e^{\mathrm{T}}\boldsymbol{q}_e{}^{\mathrm{T}}\boldsymbol{N}_4^{\mathrm{T}}\boldsymbol{N}_3-\frac{1}{2}\sum_{i=1}^{3} m_i\boldsymbol{q}^{\mathrm{T}}\boldsymbol{S}\boldsymbol{q}\cdot\boldsymbol{N}_4+\sum_{i=1}^{3} m_i\boldsymbol{B}_e^{\mathrm{T}}\boldsymbol{q}_e{}^{\mathrm{T}}\boldsymbol{N}_4^{\mathrm{T}}\cdot\boldsymbol{q}^{\mathrm{T}}\boldsymbol{S}\Big]\mathrm{d}\overline{x} \end{aligned} \tag{A2}$$

$$\boldsymbol{M}_{21}=\boldsymbol{M}_{12}^{\mathrm{T}} \tag{A3}$$

$$\begin{aligned} \boldsymbol{M}_{22}{}^{(e)} = \; & \int_0^{L_e}\Big[m_1\boldsymbol{N}_1^{\mathrm{T}}\boldsymbol{N}_1+m_2\boldsymbol{N}_2^{\mathrm{T}}\boldsymbol{N}_2+m_3\boldsymbol{N}_3^{\mathrm{T}}\boldsymbol{N}_3+\sum_{i=1}^{3} m_i\boldsymbol{S}\boldsymbol{q}\cdot\boldsymbol{q}^{\mathrm{T}}\boldsymbol{S} \\ & +\sum_{i=1}^{3} m_i\boldsymbol{N}_4^{\mathrm{T}}\boldsymbol{N}_4-m_1\boldsymbol{S}\boldsymbol{q}\cdot\boldsymbol{N}_1-m_1\boldsymbol{N}_1^{\mathrm{T}}\cdot\boldsymbol{q}^{\mathrm{T}}\boldsymbol{S}-m_2\boldsymbol{S}\boldsymbol{q}\cdot\boldsymbol{N}_2-m_2\boldsymbol{N}_2^{\mathrm{T}}\cdot\boldsymbol{q}^{\mathrm{T}}\boldsymbol{S} \\ & -m_3\boldsymbol{S}\boldsymbol{q}\cdot\boldsymbol{N}_3-m_3\boldsymbol{N}_3^{\mathrm{T}}\cdot\boldsymbol{q}^{\mathrm{T}}\boldsymbol{S}\big]\mathrm{d}\overline{x} \end{aligned} \tag{A4}$$

$$\begin{aligned} Q_\theta^{(e)} = \; & F_\tau-\dot{\theta}\int_0^{L_e}\big[2m_1\boldsymbol{B}_e^{\mathrm{T}}\boldsymbol{q}_e{}^{\mathrm{T}}\boldsymbol{N}_1^{\mathrm{T}}\boldsymbol{N}_1\dot{\boldsymbol{q}}_e\boldsymbol{B}_e+2m_2\boldsymbol{B}_e^{\mathrm{T}}\boldsymbol{q}_e{}^{\mathrm{T}}\boldsymbol{N}_2^{\mathrm{T}}\boldsymbol{N}_2\dot{\boldsymbol{q}}_e\boldsymbol{B}_e+2m_3\boldsymbol{B}_e^{\mathrm{T}}\boldsymbol{q}_e{}^{\mathrm{T}}\boldsymbol{N}_3^{\mathrm{T}}\boldsymbol{N}_3\dot{\boldsymbol{q}}_e\boldsymbol{B}_e \\ & +\sum_{i=1}^{3} m_i\boldsymbol{q}^{\mathrm{T}}\boldsymbol{S}\boldsymbol{q}\cdot\boldsymbol{q}^{\mathrm{T}}\boldsymbol{S}\dot{\boldsymbol{q}}-m_1\boldsymbol{q}^{\mathrm{T}}\boldsymbol{S}\boldsymbol{q}\cdot\boldsymbol{N}_1\dot{\boldsymbol{q}}_e\boldsymbol{B}_e-2m_1\boldsymbol{B}_e^{\mathrm{T}}\boldsymbol{q}_e{}^{\mathrm{T}}\boldsymbol{N}_1^{\mathrm{T}}\cdot\boldsymbol{q}^{\mathrm{T}}\boldsymbol{S}\dot{\boldsymbol{q}}-m_2\boldsymbol{q}^{\mathrm{T}}\boldsymbol{S}\boldsymbol{q}\cdot\boldsymbol{N}_2\dot{\boldsymbol{q}}_e\boldsymbol{B}_e \\ & -2m_2\boldsymbol{B}_e^{\mathrm{T}}\boldsymbol{q}_e{}^{\mathrm{T}}\boldsymbol{N}_2^{\mathrm{T}}\cdot\boldsymbol{q}^{\mathrm{T}}\boldsymbol{S}\dot{\boldsymbol{q}}-m_3\boldsymbol{q}^{\mathrm{T}}\boldsymbol{S}\boldsymbol{q}\cdot\boldsymbol{N}_3\dot{\boldsymbol{q}}_e\boldsymbol{B}_e-2m_3\boldsymbol{B}_e^{\mathrm{T}}\boldsymbol{q}_e{}^{\mathrm{T}}\boldsymbol{N}_3^{\mathrm{T}}\cdot\boldsymbol{q}^{\mathrm{T}}\boldsymbol{S}\dot{\boldsymbol{q}} \\ & +2m_1(R+x_e+\overline{x})\boldsymbol{N}_1\dot{\boldsymbol{q}}_e\boldsymbol{B}_e+2m_2(R+x_e+\overline{x})\boldsymbol{N}_2\dot{\boldsymbol{q}}_e\boldsymbol{B}_e+2m_3(R+x_e+\overline{x})\boldsymbol{N}_3\dot{\boldsymbol{q}}_e\boldsymbol{B}_e \\ & -2\sum_{i=1}^{3} m_i(R+x_e+\overline{x})\boldsymbol{q}^{\mathrm{T}}\boldsymbol{S}\dot{\boldsymbol{q}}+2\sum_{i=1}^{3} m_i\boldsymbol{q}_e^{\mathrm{T}}\boldsymbol{N}_4^{\mathrm{T}}\boldsymbol{N}_4\dot{\boldsymbol{q}}_e\boldsymbol{B}_e\Big]\mathrm{d}\overline{x} \\ & -\int_0^{L_e}\sum_{i=1}^{3} m_i\boldsymbol{B}_e^{\mathrm{T}}\boldsymbol{q}_e{}^{\mathrm{T}}\boldsymbol{N}_4^{\mathrm{T}}\cdot\dot{\boldsymbol{q}}^{\mathrm{T}}\boldsymbol{S}\dot{\boldsymbol{q}}\,\mathrm{d}\overline{x} \end{aligned} \tag{A5}$$

$$
\begin{aligned}
\boldsymbol{Q}_q^{(e)} = \; & \boldsymbol{Q}_p^{(e)} + \dot{\theta}^2 \int_0^{L_e} \Big[ m_1 \boldsymbol{N}_1^{\mathrm{T}} \boldsymbol{N}_1 \boldsymbol{q}_e + m_2 \boldsymbol{N}_2^{\mathrm{T}} \boldsymbol{N}_2 \boldsymbol{q}_e + m_3 \boldsymbol{N}_3^{\mathrm{T}} \boldsymbol{N}_3 \boldsymbol{q}_e + \frac{1}{2} \sum_{i=1}^{3} m_i \boldsymbol{S}\boldsymbol{q} \cdot \boldsymbol{q}^{\mathrm{T}} \boldsymbol{S}\boldsymbol{q} \\
& - \frac{1}{2} m_1 \boldsymbol{N}_1^{\mathrm{T}} \cdot \boldsymbol{q}^{\mathrm{T}} \boldsymbol{S}\boldsymbol{q} - m_1 \boldsymbol{S}\boldsymbol{q} \cdot \boldsymbol{N}_1 \boldsymbol{q}_e \boldsymbol{B}_e - \frac{1}{2} m_2 \boldsymbol{N}_2^{\mathrm{T}} \cdot \boldsymbol{q}^{\mathrm{T}} \boldsymbol{S}\boldsymbol{q} - m_2 \boldsymbol{S}\boldsymbol{q} \cdot \boldsymbol{N}_2 \boldsymbol{q}_e \boldsymbol{B}_e \\
& - \frac{1}{2} m_3 \boldsymbol{N}_3^{\mathrm{T}} \cdot \boldsymbol{q}^{\mathrm{T}} \boldsymbol{S}\boldsymbol{q} - m_3 \boldsymbol{S}\boldsymbol{q} \cdot \boldsymbol{N}_3 \boldsymbol{q}_e \boldsymbol{B}_e + m_1 (R + x_e + \overline{x}) \boldsymbol{N}_1^{\mathrm{T}} + m_2 (R + x_e + \overline{x}) \boldsymbol{N}_2^{\mathrm{T}} \\
& + m_3 (R + x_e + \overline{x}) \boldsymbol{N}_3^{\mathrm{T}} - \sum_{i=1}^{3} m_i (R + x_e + \overline{x}) \boldsymbol{S}\boldsymbol{q} + \sum_{i=1}^{3} m_i \boldsymbol{N}_4^{\mathrm{T}} \boldsymbol{N}_4 \boldsymbol{q}_e \boldsymbol{B}_e \Big] \mathrm{d}\overline{x} \\
& + 2\dot{\theta} \int_0^{L_e} \big[ m_1 \boldsymbol{N}_1^{\mathrm{T}} \boldsymbol{N}_4 \dot{\boldsymbol{q}}_e \boldsymbol{B}_e - m_1 \boldsymbol{N}_4^{\mathrm{T}} \boldsymbol{N}_1 \dot{\boldsymbol{q}}_e \boldsymbol{B}_e + m_2 \boldsymbol{N}_2^{\mathrm{T}} \boldsymbol{N}_4 \dot{\boldsymbol{q}}_e \boldsymbol{B}_e - m_2 \boldsymbol{N}_4^{\mathrm{T}} \boldsymbol{N}_2 \dot{\boldsymbol{q}}_e \boldsymbol{B}_e \\
& + m_3 \boldsymbol{N}_3^{\mathrm{T}} \boldsymbol{N}_4 \dot{\boldsymbol{q}}_e \boldsymbol{B}_e - m_3 \boldsymbol{N}_4^{\mathrm{T}} \boldsymbol{N}_3 \dot{\boldsymbol{q}}_e \boldsymbol{B}_e - \sum_{i=1}^{3} m_i \boldsymbol{S}\boldsymbol{q} \cdot \boldsymbol{N}_4 \dot{\boldsymbol{q}}_e \boldsymbol{B}_e + \sum_{i=1}^{3} m_i \boldsymbol{N}_4^{\mathrm{T}} \cdot \boldsymbol{q}^{\mathrm{T}} \boldsymbol{S}\dot{\boldsymbol{q}} \Big] \mathrm{d}\overline{x} \\
& + \int_0^{L_e} \Big[ - \sum_{i=1}^{3} m_i \boldsymbol{S}\boldsymbol{q} \cdot \dot{\boldsymbol{q}}^{\mathrm{T}} \boldsymbol{S}\dot{\boldsymbol{q}} + m_1 \boldsymbol{N}_1^{\mathrm{T}} \cdot \dot{\boldsymbol{q}}^{\mathrm{T}} \boldsymbol{S}\dot{\boldsymbol{q}} + m_2 \boldsymbol{N}_2^{\mathrm{T}} \cdot \dot{\boldsymbol{q}}^{\mathrm{T}} \boldsymbol{S}\dot{\boldsymbol{q}} + m_3 \boldsymbol{N}_3^{\mathrm{T}} \cdot \dot{\boldsymbol{q}}^{\mathrm{T}} \boldsymbol{S}\dot{\boldsymbol{q}} \Big] \mathrm{d}\overline{x} \\
& - \sum_{i=1}^{3} E_i I_i \int_0^{L_e} \boldsymbol{N}_4{''}^{\mathrm{T}} \boldsymbol{N}_4{''} \boldsymbol{q}_e \boldsymbol{B}_e \mathrm{d}\overline{x} - E_1 A_1 \int_0^{L_e} \boldsymbol{N}_1{'}^{\mathrm{T}} \boldsymbol{N}_1{'} \boldsymbol{q}_e \boldsymbol{B}_e \mathrm{d}\overline{x} \\
& - E_2 A_2 \int_0^{L_e} \boldsymbol{N}_2{'}^{\mathrm{T}} \boldsymbol{N}_2{'} \boldsymbol{q}_e \boldsymbol{B}_e \mathrm{d}\overline{x} - E_3 A_3 \int_0^{L_e} \boldsymbol{N}_3{'}^{\mathrm{T}} \boldsymbol{N}_3{'} \boldsymbol{q}_e \boldsymbol{B}_e \mathrm{d}\overline{x} - G^* A_2 \int_0^{L_e} \boldsymbol{N}_6{}^{\mathrm{T}} \boldsymbol{N}_6 \boldsymbol{q}_e \boldsymbol{B}_e \mathrm{d}\overline{x}
\end{aligned} \tag{A6}
$$

## Appendix B. The Matrices in Equation (33)

$$
\begin{aligned}
\widetilde{\boldsymbol{M}}_{22}{}^{(e)} = \; & \int_0^{L_e} \big[ m_1 \boldsymbol{B}_e^{\mathrm{T}} \boldsymbol{N}_1{}^{\mathrm{T}} \boldsymbol{N}_1 \boldsymbol{B}_e + m_2 \boldsymbol{B}_e^{\mathrm{T}} \boldsymbol{N}_2{}^{\mathrm{T}} \boldsymbol{N}_2 \boldsymbol{B}_e + m_3 \boldsymbol{B}_e^{\mathrm{T}} \boldsymbol{N}_3{}^{\mathrm{T}} \boldsymbol{N}_3 \boldsymbol{B}_e \\
& + \sum_{i=1}^{3} m_i \boldsymbol{B}_e^{\mathrm{T}} \boldsymbol{N}_4{}^{\mathrm{T}} \boldsymbol{N}_4 \boldsymbol{B}_e \Big] \mathrm{d}\overline{x}
\end{aligned} \tag{A7}
$$

$$
\begin{aligned}
\widetilde{\boldsymbol{G}}_{22}{}^{(e)} = \; & - K_d \Big( \boldsymbol{Q}_{pf} + \boldsymbol{Q}_{pm} \Big) - 2\Omega \cdot \int_0^{L_e} \big( m_1 \boldsymbol{N}_1^{\mathrm{T}} \boldsymbol{N}_4 - m_1 \boldsymbol{N}_4^{\mathrm{T}} \boldsymbol{N}_1 + m_2 \boldsymbol{N}_2^{\mathrm{T}} \boldsymbol{N}_4 - m_2 \boldsymbol{N}_4^{\mathrm{T}} \boldsymbol{N}_2 \\
& + m_3 \boldsymbol{N}_3^{\mathrm{T}} \boldsymbol{N}_4 - m_3 \boldsymbol{N}_4^{\mathrm{T}} \boldsymbol{N}_3 \big) \mathrm{d}\overline{x}
\end{aligned} \tag{A8}
$$

$$
\begin{aligned}
\widetilde{\boldsymbol{K}}_{22}^{(e)} = \; & - K_p \Big( \boldsymbol{Q}_{pf} + \boldsymbol{Q}_{pm} \Big) - \Omega^2 \int_0^{L_e} \big[ m_1 \boldsymbol{B}_e^{\mathrm{T}} \boldsymbol{N}_1^{\mathrm{T}} \boldsymbol{N}_1 \boldsymbol{B}_e + m_2 \boldsymbol{B}_e^{\mathrm{T}} \boldsymbol{N}_2^{\mathrm{T}} \boldsymbol{N}_2 \boldsymbol{B}_e \\
& + m_3 \boldsymbol{B}_e^{\mathrm{T}} \boldsymbol{N}_3^{\mathrm{T}} \boldsymbol{N}_3 \boldsymbol{B}_e + \sum_{i=1}^{3} m_i \boldsymbol{B}_e^{\mathrm{T}} \boldsymbol{N}_4^{\mathrm{T}} \boldsymbol{N}_4 \boldsymbol{B}_e - \sum_{i=1}^{3} m_i (R + x_e + x) \boldsymbol{S} \Big] \mathrm{d}\overline{x} \\
& + \sum_{i=1}^{3} E_i I_i \int_0^{L_e} \boldsymbol{B}_e^{\mathrm{T}} \boldsymbol{N}_4{''}^{\mathrm{T}} \boldsymbol{N}_4{''} \boldsymbol{B}_e \mathrm{d}\overline{x} \\
& + E_1 A_1 \int_0^{L_e} \boldsymbol{B}_e^{\mathrm{T}} \boldsymbol{N}_1{'}^{\mathrm{T}} \boldsymbol{N}_1{'} \boldsymbol{B}_e \mathrm{d}\overline{x} + E_2 A_2 \int_0^{L_e} \boldsymbol{B}_e^{\mathrm{T}} \boldsymbol{N}_2{'}^{\mathrm{T}} \boldsymbol{N}_2{'} \boldsymbol{B}_e \mathrm{d}\overline{x} \\
& + E_3 A_3 \int_0^{L_e} \boldsymbol{B}_e^{\mathrm{T}} \boldsymbol{N}_3{'}^{\mathrm{T}} \boldsymbol{N}_3{'} \boldsymbol{B}_e \mathrm{d}\overline{x} + G^* A_2 \int_0^{L_e} \boldsymbol{B}_e^{\mathrm{T}} \boldsymbol{N}_6{}^{\mathrm{T}} \boldsymbol{N}_6 \boldsymbol{B}_e \mathrm{d}\overline{x}
\end{aligned} \tag{A9}
$$

## References


1. Ma, H.W.; Sun, W.; Du, D.; Liu, X.F.; Liu, H.H. Nonlinear vibration analysis of double cylindrical shells coupled structure with bolted connection and partially attached constrained layer damping. *Int. J. Mech. Sci.* **2022**, *223*, 107270. [CrossRef]
2. Li, H.; Wang, Z.H.; Lv, H.Y.; Zhou, Z.X.; Han, Q.K.; Liu, J.G. Nonlinear vibration analysis of fiber reinforced composite cylindrical shells with partial constrained layer damping treatment. *Thin-Walled Struct.* **2020**, *157*, 107000. [CrossRef]
3. Cai, C.; Zheng, H.; Liu, G.R. Vibration analysis of a beam with PCLD patch. *Appl. Acoust.* **2004**, *65*, 1057–1076. [CrossRef]
4. Zheng, H.; Tan, X.M.; Cai, C. Damping analysis of beams covered with multiple PCLD patches. *Int. J. Mech. Sci.* **2006**, *48*, 1371–1383. [CrossRef]
5. Zheng, H.; Cai, C.; Pau, G.S.H.; Liu, G.R. Minimizing vibration response of cylindrical shells through layout optimization of passive constrained layer damping treatments. *J. Sound Vib.* **2005**, *279*, 739–756. [CrossRef]
6. Zheng, L.; Qiu, Q.; Wan, H.; Zhang, D.D. Damping analysis of multilayer passive constrained layer damping on cylindrical shell using transfer function method. *J. Vib. Acoust.* **2014**, *136*, 031001. [CrossRef]
7. Zhang, Q.J.; Sainsbury, M.G. The Galerkin element method applied to the vibration of rectangular damped sandwich plates. *Comput. Struct.* **2000**, *74*, 717–730. [CrossRef]
8. Gröhlich, M.; Böswald, M.; Wallaschek, J. Viscoelastic damping design—A novel approach for shape optimization of Constrained Layer Damping treatments at different ambient temperatures. *J. Sound Vib.* **2023**, *555*, 117703. [CrossRef]
9. Baz, A.; Ro, J. Optimum design and control of active constrained layer damping. *J. Vib. Acoust.* **1995**, *117*, 135–144. [CrossRef]

10. Baz, A. *Active and Passive Vibration Damping*; John Wiley & Sons, Inc.: Hoboken, NJ, USA, 2019.
11. Varadan, V.V.; Lim, Y.H.; Varadan, V.K. Closed loop finite-element modeling of active/passive damping in structural vibration control. *Smart Mater. Struct.* **1996**, *5*, 685–694. [CrossRef]
12. Fung, E.H.K.; Yau, D.T.W. Vibration characteristics of a rotating flexible arm with ACLD treatment. *J. Sound Vib.* **2004**, *269*, 165–182. [CrossRef]
13. Lee, J.T. Active structural acoustics control of beams using active constrained layer damping through loss factor maximization. *J. Sound Vib.* **2005**, *287*, 481–503. [CrossRef]
14. Sharnappa, N.; Ganesan, N.; Sethuraman, R. Dynamic modeling of active constrained layer damping of composite beam under thermal environment. *J. Sound Vib.* **2007**, *305*, 728–749. [CrossRef]
15. Vasques, C.M.A.; Rodrigues, J.D. Combined feedback/feedforward active control of vibration of beams with ACLD treatments: Numerical simulation. *Comput. Struct.* **2008**, *86*, 292–306. [CrossRef]
16. Boudaoud, H.; Daya, E.M.; Belouettar, S.; Duigou, L.; Potier-Ferry, M. Damping analysis of beams submitted to passive and active control. *Eng. Struct.* **2009**, *31*, 322–331. [CrossRef]
17. Kumar, N.; Singh, S.P. Vibration and damping characteristics of beams with active constrained layer treatments under parametric variations. *Mater. Des.* **2009**, *30*, 4162–4174. [CrossRef]
18. Kumar, S.; Kumar, R. Theoretical and experimental vibration analysis of rotating beams with combined ACLD and Stressed Layer Damping treatment. *Appl. Acoust.* **2013**, *74*, 675–693. [CrossRef]
19. Panda, R.K.; Nayak, B.; Sarangi, S.K. Active Vibration Control of Smart Functionally Graded Beams. *Procedia Eng.* **2016**, *144*, 551–559. [CrossRef]
20. Li, L.; Zhang, D.G.; Guo, Y.B. Dynamic modeling and analysis of a rotating flexible beam with smart ACLD treatment. *Compos. Part B Eng.* **2017**, *131*, 221–236. [CrossRef]
21. Guo, Y.B.; Li, L.; Zhang, D.G. Dynamic modeling and vibration analysis of rotating beams with active constrained layer damping treatment in temperature field. *Compos. Struct.* **2019**, *226*, 111217. [CrossRef]
22. Mishra, V.N.; Sarangi, S.K. Augmented active constrained layer damping of beams using graphite reinforced viscoelastic composite material. *Mech. Adv. Mater. Struct.* **2022**, 1–14. [CrossRef]
23. Li, M.; Sun, W.; Liu, Y.; Ma, H.W. Influence analysis of control signal phase on the vibration reduction effect of active constrained layer damping. *Appl. Acoust.* **2022**, *190*, 108658. [CrossRef]
24. Park, C.H.; Baz, A. Vibration control of bending modes of plates using active constrained layer damping. *J. Sound Vib.* **1999**, *227*, 711–734. [CrossRef]
25. Li, L.; Liao, W.H.; Zhang, D.G.; Guo, Y.B. Vibration analysis of a free moving thin plate with fully covered active constrained layer damping treatment. *Compos. Struct.* **2020**, *235*, 111742. [CrossRef]
26. Kattimani, S.C.; Ray, M.C. Vibration control of multiferroic fibrous composite plates using active constrained layer damping. *Mech. Syst. Signal Process.* **2018**, *106*, 334–354. [CrossRef]
27. Pani, S.; Behera, D.K. Active constrained layer damping treatment on graphene reinforced composite plates. *Mater. Today Proc.* **2020**, *33*, 5206–5212. [CrossRef]
28. Kallannavar, V.; Kattimani, S. Effect of temperature on the performance of active constrained layer damping of skew sandwich plate with CNT reinforced composite core. *Mech. Adv. Mater. Struct.* **2022**, *29*, 5423–5442. [CrossRef]
29. Zhao, J.; Wong, P.K.; Ma, X.; Xie, Z.C.; Xu, J.; Cristino, V.A. Simplification of finite element modeling for plates structures with constrained layer damping by using single-layer equivalent material properties. *Compos. Part B Eng.* **2019**, *157*, 283–288. [CrossRef]
30. Zhai, J.Y.; Li, J.W.; Wei, D.T.; Gao, P.X.; Yan, Y.Y.; Han, Q.K. Vibration control of an aero pipeline system with active constraint layer damping treatment. *Appl. Sci.* **2019**, *9*, 2094. [CrossRef]
31. Zhang, Y.L.; Liu, X.F.; Rong, W.C.; Gao, P.X.; Yu, T.; Han, H.W.; Xu, L.J. Vibration and damping analysis of pipeline system based on partially piezoelectric active constrained layer damping treatment. *Materials* **2021**, *14*, 1209. [CrossRef]
32. Vinyas, M. Vibration control of skew magneto-electro-elastic plates using active constrained layer damping. *Compos. Struct.* **2019**, *208*, 600–617. [CrossRef]
33. Vinyas, M.; Harursampath, D.; Nguyen-Thoi, T. Influence of active constrained layer damping on the coupled vibration response of functionally graded magneto-electro-elastic plates with skewed edges. *Def. Technol.* **2020**, *16*, 1019–1038. [CrossRef]
34. Liao, W.H.; Wang, K.W. A new active constrained layer configuration with enhanced boundary actions. *Smart Mater. Struct.* **1996**, *5*, 638–648. [CrossRef]
35. Liao, W.H.; Wang, K.W. Characteristics of enhanced active constrained layer damping treatments with edge elements, Part 1: Finite element model development and validation. *ASME J. Vib. Acoust.* **1998**, *120*, 886–893. [CrossRef]
36. Liao, W.H.; Wang, K.W. Characteristics of enhanced active constrained layer damping treatments with edge elements, Part 2: System analysis. *ASME J. Vib. Acoust.* **1998**, *120*, 894–900. [CrossRef]
37. Gao, J.X.; Liao, W.H. Damping Characteristics of beams with enhanced self-sensing active constrained layer treatments under various boundary conditions. *J. Vib. Acoust.* **2005**, *127*, 173–187. [CrossRef]
38. Jin, C.Z.; Li, L.; Zhang, D.G.; Zhang, Y. Dynamic modeling and vibration control of a rotating space flexible arm with enhanced active constrained layer damping treatment. *IOP Conf. Ser. Mater. Sci. Eng.* **2019**, *531*, 012071. [CrossRef]

39. Li, L.; Liao, W.H.; Zhang, D.G.; Guo, Y.B. Dynamic modeling and analysis of rotating beams with partially covered enhanced active constrained layer damping treatment. *J. Sound Vib.* **2019**, *455*, 46–68. [CrossRef]
40. Fang, Y.; Li, L.; Zhang, D.G.; Chen, S.J.; Liao, W.H. Vibration suppression of a rotating functionally graded beam with enhanced active constrained layer damping treatment in temperature field. *Thin-Walled Struct.* **2021**, *161*, 107522. [CrossRef]
41. Gupta, M.; Ray, M.C.; Patil, N.D.; Kundalwal, S.I. Dynamic modelling and analysis of smart carbon nanotube-based hybrid composite beams: Analytical and finite element study. *Proc. Inst. Mech. Eng. Part L J. Mater. Des. Appl.* **2021**, *235*, 2185–2206. [CrossRef]
42. Jiang, F.; Li, L.; Liao, W.H.; Zhang, D.G. Vibration control of a rotating hub-plate with enhanced active constrained layer damping treatment. *Aerosp. Sci. Technol.* **2021**, *118*, 107081. [CrossRef]
43. Tao, W.; Jiang, F.; Li, L.; Zhang, D.; Guo, X.; Liao, W.-H. Dynamical analysis and vibration estimation of a flexible plate with enhanced active constrained layer damping treatment by combinatorial neural networks of surrogates. *Aerosp. Sci. Technol.* **2023**, *133*, 108136. [CrossRef]
44. Plunkett, R.; Lee, C.T. Length optimization for constrained viscoelastic layer damping. *J. Acoust. Soc. Am.* **1970**, *48*, 150–161. [CrossRef]
45. Kress, G. Improving single-constrained-layer damping treatment by sectioning the constraining layer. *Am. Soc. Mech. Eng.* **1987**, *5*, 41–48.
46. Lesieutre, G.A.; Lee, U. A finite element for beams having segmented active constrained layers with frequency-dependent viscoelastics. *Smart Mater. Struct.* **1996**, *5*, 615–627. [CrossRef]
47. Kapadia, R.K.; Kawiecki, G. Experimental evaluation of segmented active constrained layer damping treatments. *J. Intell. Mater. Syst. Struct.* **1997**, *8*, 103–111. [CrossRef]
48. Trompette, P.; Fatemi, J. Damping of beams. Optimal distribution of cuts in the viscoelastic constrained layer. *Struct. Optim.* **1997**, *3*, 167–171. [CrossRef]
49. Liu, Q.; Chattopadhyay, A.; Gu, H.; Zhou, X. Use of segmented constrained layer damping treatment for improved helicopter aeromechanical stability. *Smart Mater. Struct.* **2000**, *9*, 523–532. [CrossRef]
50. Chattopadhyay, A.; Gu, H.Z.; Beri, R. Modeling segmented active constrained layer damping using hybrid displacement field. *AIAA J.* **2001**, *39*, 480–486. [CrossRef]
51. Cento, P.F.; Kawiecki, G. Finite element modeling of segmented active constrained damping layers including bonding layer effect. *J. Vib. Control* **2002**, *8*, 805–832. [CrossRef]
52. Al-Ajmi, M.A.; Bourisli, R.I. Optimum design of segmented passive-constrained layer damping treatment through genetic algorithms. *Mech. Adv. Mater. Struct.* **2008**, *15*, 250–257. [CrossRef]
53. Grégoire, L.; Gerald, K. Optimization of segmented constrained layer damping with mathematical programming using strain energy analysis and modal data. *Mater. Des.* **2010**, *31*, 14–24.
54. Avinash, K.; Pravin, H. Optimization of segmented constrained layer damping literature review. *Int. J. Eng. Adv. Technol.* **2014**, *3*, 151–153.
55. Tian, S.T.; Xu, Z.; Wu, Q.; Qin, C. Dimensionless analysis of segmented constrained layer damping treatments with modal strain energy method. *Shock Vib.* **2016**, *2016*, 8969062. [CrossRef]
56. Chinonso, O.U. *Experimental Study of Segmented Constrained Layer Damping in Rectangular and Sinusoidal Beams*; University of Maryland: College Park, MD, USA, 2020.